

Alexandra Ploner

Synthesis and investigation of electrolytes for rechargeable Mg-ion batteries

MASTER THESIS

For obtaining the academic degree
Diplom-Ingenieurin

Master Programme of
Advanced Materials Science



Graz University of Technology

Supervisor:

Assoc.Prof. Dipl.-Chem. Dr.rer.nat. Bernhard Gollas
Institute for Chemistry and Technology of Materials

Graz, January 2015

EIDESSTATTLICHE ERKLÄRUNG AFFIDAVIT

Ich erkläre an Eides statt, dass ich die vorliegende Arbeit selbstständig verfasst, andere als die angegebenen Quellen/Hilfsmittel nicht benutzt, und die den benutzten Quellen wörtlich und inhaltlich entnommenen Stellen als solche kenntlich gemacht habe. Das in TUGRAZonline hochgeladene Textdokument ist mit der vorliegenden Masterarbeit identisch.

I declare that I have authored this thesis independently, that I have not used other than the declared sources / resources, and that I have explicitly indicated all material which has been quoted either literally or by content from the sources used. The text document uploaded to TUGRAZonline is identical to the present master thesis.

.....
Datum/date

.....
Unterschrift/signature

DANKSAGUNG
ACKNOWLEDGEMENT

KURZFASSUNG

Elektrochemische Speicher – Batterien und Akkumulatoren – mit hohen Energiedichten sind von besonderem Interesse derzeitiger Forschung vor allem im Bereich der Automobilindustrie. Magnesium als kostengünstiges und umweltfreundliches Metall kann aufgrund dendritfreier Metallabscheidung in metallischer Form als Anode in Batterien eingesetzt werden und ermöglicht so hohe Energiedichten. Als zweiwertiges Kation speichert es doppelt so viel elektrische Energie pro Volumen wie Lithium.

Die Entwicklung von stabilen Elektrolyten (>3 V vs. Mg/Mg²⁺), die reversible Metallabscheidung erlauben, steht im Vordergrund dieser Diplomarbeit. Zurzeit bestimmen sie den Fortschritt in der Entwicklung der Magnesium-Ionen Batterie und legen das Potential für kompatible Kathodenmaterialien fest. Es wurden geeignete Elektrolyte synthetisiert und parallel dazu elektrochemische Eigenschaften wie kathodische/anodische Stabilität, Diffusionskoeffizienten und Reversibilität verschiedener Elektrolyte bestimmt. Heterokern-NMR wurde eingesetzt um die Identität vorhandener Spezies im Elektrolyt zu klären. Außerdem wurden niedrig legierte Magnesiummaterialien in einem ausgewählten Elektrolyt zyklisiert um die Einflüsse der Legierungselemente auf das Auflösungs- und Abscheidungsvermögen von Magnesium zu analysieren.

ABSTRACT

Electrochemical energy storage devices – batteries and accumulators – with high energy densities are of particular interest in current research, especially for electronic vehicles. Magnesium being cheap and environmentally friendly can be used as anode in metallic form due to non dendritic metal deposition. This allows high energy densities. Since magnesium is a divalent cation its theoretical volumetric electrical energy is twice that of lithium.

The development of stable electrolytes (>3 V vs. Mg/Mg²⁺) which allow reversible magnesium deposition is the main focus of this diploma thesis. At the moment they determine the progress in the field of magnesium ion batteries and specify the potential of compatible cathode materials. Suitable electrolytes were synthesized and electrochemical properties such as cathodic/anodic stabilities, diffusion coefficients and the reversibility of magnesium deposition/dissolution were investigated. Multinuclear NMR was used to learn more about the identity of existing ion species in solutions. Additionally, different low alloyed magnesium materials were cycled in a suitable electrolyte to investigate the influence of various alloying elements on the deposition/ dissolution process of magnesium.

ABBREVIATIONS

acac	acetyl acetate
APC	all phenyl complex
b.p.	boiling point
BCF	tris(pentafluorophenyl)borane
BMIMBF ₄	1-butyl-3-methylimidazolium tetrafluoroborate
CE	current efficiency, counter electrode
CV	cyclic voltammetry
DEMETFSI	diethylmethyl-(2-methoxyethyl) ammonium bis(trifluoromethylsulfonyl)imide
EC	ethylen carbonate
EMITFSI	1-ethyl-3-methylimidazolium bis(trifluoromethylsulfonyl)imide
GC	gas chromatography, glassy carbon
h ⁺	hole
HFP	hexafluoropropylene
HMDS	hexamethyldisilazide magnesium chloride
HPLC	high pressure liquid chromatography
m.p.	melting point
MACC	magnesium aluminum chloride complex
MS	mass spectrometry
NMR	nuclear magnetic resonance
OCP	open circuit potential
ORTEP	Oak Ridge Thermal Ellipsoid Plot
PAN	polyacrylnitrile
PC	propylene carbonate
PEO	polyethylene oxide
PhMgCl	phenylmagnesiumchloride
PMMA	polymethylmethacrylate
PP13-TFSI	N-methyl-N-propylpiperidinium bistrifluoromethanesulfonylimide
Pt	platinum
PVdF	polyvinylidene fluoride

RDE	rotating disk electrode
RE	reference electrode
SCXRD	single crystal x-ray diffraction
SPEU	segmented polyetherurethane
TG	tetraglyme
THF	tetrahydrofuran
TPBA	tetraphenylborate anion
WE	working electrode
wt.%	weight percentage

<i>A</i>	electrode area
<i>D</i>	diffusion coefficient
<i>E</i>	potential
<i>i</i>	current
<i>j</i>	current density
<i>T</i>	temperature
<i>v</i>	scan rate
δ	chemical shift
η	dynamic viscosity
<i>d</i>	diameter

CONTENT

1	Introduction	1
1.1	Batteries used in road vehicles	1
1.2	Rechargeable magnesium-ion battery	3
1.2.1	Benefits and disadvantages of Mg	3
1.2.2	Anodes	4
1.2.3	Cathodes	4
1.2.4	Electrolytes	5
2	Methods	10
2.1	Multinuclear NMR	10
2.1.1	¹¹ Boron	10
2.1.2	²⁷ Aluminum	11
2.1.3	¹⁹ Fluorine	12
2.2	Electrochemical methods	12
2.2.1	Cyclic voltammetry	12
2.2.2	Chronoamperometry	13
3	Objective	14
4	Experimental part	15
4.1	Chemicals and materials	15
4.1.1	Chemicals	15
4.1.2	Anode materials	16
4.1.3	Equipment	16
4.2	Synthesis	17
4.2.1	Triphenylborane – Halide approach	17
4.2.2	Triphenylborane – Grignard approach	17
4.2.3	HPLC	18
4.2.4	GC/MS analysis	18
4.3	Electrolyte preparation	19
4.3.1	General	19
4.3.2	PhMgCl	19
4.3.3	1:2 all phenyl complex (APC)	19
4.3.4	BCF-PhMgCl electrolyte	20
4.3.5	Saturated magnesium aluminum chloride complex (MACC)	20
4.4	Electrolyte characterization	21
4.4.1	Cyclic voltammetry and chronoamperometry	21
4.4.2	NMR	22

5	Results and discussion	23
5.1	Synthesis	23
5.1.1	Halide approach	23
5.1.2	Grignard approach	24
5.2	Electrolyte characterization	26
5.2.1	1 M PhMgCl in THF	27
5.2.2	0.25 M APC in THF	32
5.2.3	0.2 M BCF-PhMgCl in THF	37
5.2.4	Saturated MACC in THF electrolyte	41
5.3	Characterization of anode alloys	45
5.3.1	Mg 99.9 %	45
5.3.2	MgGd	47
5.3.3	MgGdZn	49
5.4	Reference electrodes	50
6	Summary and conclusion	52

1 Introduction

These days our energy system relies mainly on primary energy resources, i.e. fossil fuels. In particular two thirds of the oil production are used for transport purposes only [1]. Since these resources continue to be consumed faster than they are created by nature, there is a tremendous demand to cover the future energy needs by renewable resources. These energy sources generate mainly electrical energy which has to be stored in energy storage devices to be able to equally distribute the energy and to make it available as soon as it is needed. A battery, as one example of such a device, stores this energy in chemical form [2]. Especially for transport applications, batteries as energy deliverer are a good alternative to fossil fuels. However, researchers are still looking for a battery system, which can store enough energy to enable a long driving range and are cheap compared to currently used car engines. The next chapter outlines several different battery systems for electric vehicles.

1.1 Batteries used in road vehicles

The key criteria for the development of secondary (rechargeable) batteries in road vehicles are as follows [3]:

- **Capacity**
In battery applications, capacity refers to the electrons that an electrochemical storage device can supply before it is totally discharged. The charge is given in terms of coulombs (As) or ampere-hours (Ah).
- **Charge-rate**
The charge-rate, also called c-rate, connects the capacity of a battery and the time needed for recharging it. So if a battery has a capacity of i.e. 1.6 Ah and the c-rate is 0.8, this means the battery can be recharged in 2h.
- **Energy and power**
Specific energy and energy density are very important parameters for battery applications, especially for road vehicles (Fig. 1). The energy storage device should combine a minimum of weight (Wh/kg) and a high energy output per volume (Wh/cm³).
- **Cycle life**
The cycle life of a battery is described by its number of cycles (charge-discharge) until its function reaches a specific percentage value of its initial state.

Currently used batteries in electrical road vehicles are lead-acid, Ni-MH, Na-S and diverse Li-ion technologies. Table 1 illustrates their properties.

Table 1: Properties of batteries designed for power applications [3].

System	Pb-acid	Nickel-Metal-Hydride	Lithium-ion
Standard voltage [V]	2.06	1.3	4.1
Operating voltage [V]	2.0	1.2	3.6
Specific energy [Wh/kg]	25-35	60	140
Energy density [Wh/l]	100	200	320
Cycle life	100-1000	1000-2500	800-2500

Lead-acid is by far the best known and oldest rechargeable battery used in automobile industry. It is mainly required for lighting and starting, but it shows a low energy density and a limited cycle life. Ni-MH based batteries were successfully implemented in hybrid vehicles because of the high cycle stability and non soluble electrode components that minimize the possibility of short circuits via dendrite formation. The specific properties of lithium ion batteries depend on their particular cathodes and their cell geometry, but they still exceed those of Ni-MH and lead-acid. However, safety problems have yet to be solved and the life span of the battery (5 years) is also not acceptable [2]. Hence, an adequate battery, which fulfils the needs for automotive applications has not been found.

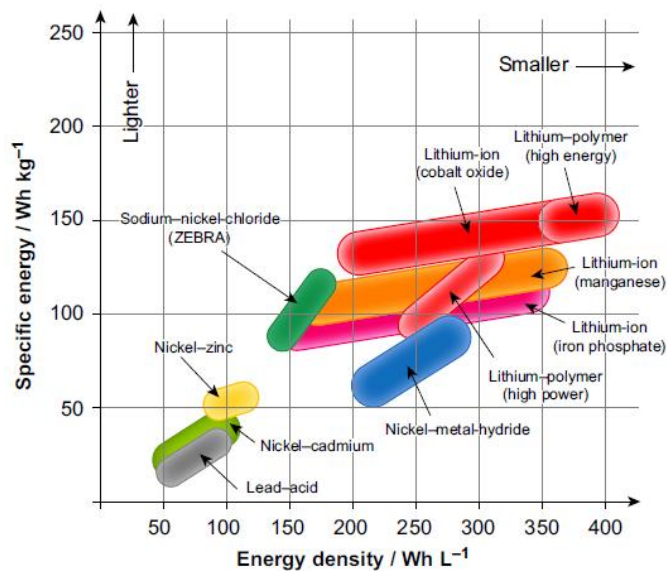


Fig. 1 Performance of different batteries in terms of specific energy and energy density [3].

The main challenge for future batteries is the optimization of the specific energy in combination with a high energy density. A promising candidate in this context would be the magnesium-ion battery. Mg – an element with a very negative standard potential – can store more electrical energy per volume than lithium due to its divalent nature. The low price of the metal and the environmental friendliness makes magnesium even more

attractive. If such a battery operates at a cell voltage of 3 V, it would be possible to achieve estimated energy densities up to 400 Wh/kg.

1.2 Rechargeable magnesium-ion battery

Magnesium has already successfully replaced zinc anodes in primary battery applications (Leclanche cell) [4]. These batteries showed a greater electrochemical window (due to more negative standard potential of Mg), a higher gravimetric energy density and medium discharge rates. But one of the biggest advantages was the long storage life of this battery, even at elevated temperatures.

Since magnesium shows the ability of intercalation/de-intercalation in solid materials, similar to lithium and sodium, the research has extended to secondary battery applications. The challenge is to find electrolytes that show reversible magnesium stripping and plating, to synthesize cathode materials which exhibit magnesitation/de-magnesitation at more than 3 V vs. Mg/Mg²⁺ and to optimize different Mg alloys or intermetallic phases for the anode.

This diploma thesis had the main focus on the development of suitable electrolytes, since they limit the progress in this field. However, for a better understanding of the complete battery system Mg will be compared to Li and a short introduction on currently investigated cathode and anode materials will be given. Then the electrolytes will be discussed.

1.2.1 Benefits and disadvantages of Mg

Modern lithium-ion batteries are the most commonly used batteries but they are nearing their limit of possible energy density. For higher Wh/kg values, the Li-C₆ intercalation anode has to be replaced by pure lithium metal electrodes [5]. Non commercial technologies such as Li-S or Li-air, are also facing several problems. Therefore it is worthwhile to develop a magnesium based battery. The benefits and drawbacks of magnesium compared to lithium are shown in Table 2:

Table 2: Properties of lithium and magnesium for battery applications [5].

Property	Li	Mg
Standard potential [V]	-3.01	-2.37
Gravimetric capacity [Ah/g]	3.86	2.20
Volumetric capacity [Ah/cm ³]	2.06	3.8
Reactivity	highly reactive	less reactive
Abundance	0.002 %	2.75 %[6]
Metal deposition	dendrites	no dendrites
Environmental toxicity	toxic for endotherm	non-toxic

The disadvantages of magnesium compared to lithium are basically the less negative standard potential and the lower charge output per mass which is nearly the half of lithium. But for the usage in electric vehicles the space saving per charge is up to 50% and there is no safety issue related to dendrite formation. Concerning the costs, magnesium is far less expensive than lithium due to its abundance in the earth's crust.

1.2.2 Anodes

The first magnesium battery prototypes had as anodes **pure (99.9 %) magnesium** foils [7]. Other attempts were made with nano-structured magnesium [8] and the Mg alloy AZ31 (3% Al, 1% Zn) [9].

A different approach – based on the ability of Mg to form intermetallic phases with other metals – was made using tin, antimony, bismuth and Sb/Bi phases as **intermetallic/alloying type anodes**. The advantage of these alloys is their compatibility with conventional electrolytes such as $\text{Mg}(\text{N}(\text{SO}_2\text{CF}_3)_2)_2$ in acetonitrile [10] since no blocking layer is formed in contrast to pure Mg. However, a loss in capacity has to be taken. The experiments with tin showed the formation of Mg_2Sn intermetallic phase during the first deposition cycle but the extraction of Mg from this phase caused the amorphization of the electrode [11]. On the other hand, experiments with Bi, showed good cycling properties [10]. The cycling capability dropped when alloying more Sb. Pure antimony led to the worst cycling performance. For all Bi, Bi/Sb and Sb based electrodes an irreversible loss on the first cycle was reported. The strong ionic bond in Mg_3Sb_2 is assumed to inhibit the extraction of Mg^{2+} from this intermetallic phase [10].

1.2.3 Cathodes

Mg, like Li, can be chemically inserted in and extracted from different inorganic solids by intercalation/de-intercalation or a displacement reaction. This property is crucial for the development of magnesium-ion batteries. Table 3 gives an overview on the different types of cathode materials developed so far.

Table 3: Different cathode types investigated for Mg-ion battery applications.

Cathode type	Structure	Example	Reference
Chevrel phase	$\text{M}_x\text{Mo}_6\text{T}_8$ (T = S, Se, Te)	Mo_6S_8	[12]
Metal oxide/sulfide/boride	M_xO_y , M_xB_y , M_xS_y	V_2O_5	[13,14]
Transition metal oxide	$\text{Mg}_x\text{M}_y\text{O}_z$	MgCo_2O_4	[15,16]
Nasicon type	$\text{A}_2(\text{PO}_4)_3$ or $\text{AB}(\text{PO}_4)_3$	$\text{Mg}_{0.5}\text{Ti}_2(\text{PO}_4)_3$	[17]
Defect oxide spinel phase		$\text{Mg}_{1.5}\text{MnO}_3$	[18]
Olivine phase	MgMSiO_4 (M = Fe, Co, Mn)	MgFeSiO_4	[19]
Mg-S conversion type		S	[20]

The **Chevrel structure** forms an open framework with pseudo-cubic cavities which is able to insert mono- and divalent cations [21]. Mo_6S_8 as an example can accommodate two Mg^{2+} ions in its lattice, so this material was investigated as possible cathode material. Experiments showed that due to charge trapping, only 70% of the cathode's total electrical capacity can be used at room temperature [22]. The Mg intercalation/de-intercalation is nearly reversible at temperatures between 60-80°C [23]. The magnesiation/de-magnesiation reaction, however, occurs at low potentials of approx. 1.1 V vs. Mg/Mg^{2+} which is a big drawback [12].

Different **metal oxides** with higher open circuit voltage vs. Mg/Mg^{2+} showed the capability to intercalate Mg-ions, but unfortunately the process seems to be irreversible [13]. For V_2O_5 reversible insertion and extraction of Mg ions was reported [24]. However, the kinetics of Mg intercalation in this solid are extremely slow [25] and traces of water are needed to solvate Mg^{2+} and to facilitate the process [14].

Similarly, **Nasicon type** electrodes show rather slow Mg intercalation [17]. Modifications of $\text{Mg}_{0.5}\text{Ti}_2(\text{PO}_4)_3$ did not improve the intercalation rate and the cycling behavior was not satisfactory [26].

A more promising system seems to be a **transition metal-oxide combination**. The transition metal oxides (TMO). MgCo_2O_4 , for example exhibit electric conductivities up to 10^{-2} mS/cm and other TMO materials are stable up to 3-3.5 V according to literature [15,16]. Other research groups, however, could not achieve reversible Mg cycling with TMO materials [18].

Other complex structures like the **defect oxide spinel MgMnO_3** or the **olivine phase MgMnSiO_4** were also investigated. MgMnO_3 shows high coulombic efficiency even after 100 cycles but the charge capacity is far lower than in theory [18]. The olivine phase MgMnSiO_4 tested with 0.25 M $\text{Mg}(\text{AlCl}_2\text{EtBu})_2$ electrolyte allows reversible magnesium incorporation at consistent discharge capacities of 80 mAh/g, and the de-intercalation reaction happens at 1.6 (vs. Mg/Mg^{2+}) [19].

In contrast to the previous mentioned cathode materials elemental sulfur can serve as a conversion cathode in a **Mg-S battery** system. This battery has a theoretical volumetric energy density of 4000 Wh/l which would be a drastical improvement [20]. However, the challenge herein is to find an electrolyte which prevents sulfur dissolution and the formation of polysulfides.

1.2.4 Electrolytes

There are two main electrolyte systems for the secondary magnesium battery: solutions based on organic solvents or ionic liquid and polymer based electrolytes. Aqueous solutions cannot be used as electrolytes since the Mg metal instantly forms a non-conductive passive layer on the surface and so no reversible Mg deposition/dissolution can take place.

1.2.4.1 Organic solvent based electrolytes

First attempts to reversibly electro-deposit Mg from simple inorganic salts such as MgCl_2 , $\text{Mg}(\text{ClO}_4)_2$ or $\text{Mg}(\text{CF}_3\text{SO}_3)_2$ dissolved in organic solvents failed because a dense passive layer formed on the electrode surface [27,28]. Mg-ions, unlike Li-ions, are unable to diffuse through these layers and therefore no reversible plating reaction occurs.

Gregory *et al.* [13] initiated the search for electrolytes for secondary battery applications investigating **Grignard reagents** which are organomagnesium halides in ethereal solution (e.g. THF). Such electrolytes show highly reversible behavior for the Mg plating process without any dendrite formation. In this context, reversibility refers to the calculated current efficiency and charge transfer kinetics (see section 5.2). The disadvantage of these solutions is their low conductivity and anodic stability. But it has been found that the anodic stability can be controlled via the R group in such Grignard reagents (RMgX) [29].

Based on this observation various electrolytes have been synthesized by mixing Lewis bases $\text{R}_x\text{MgX}_{2-x}$ with different Lewis acids. Three main electrolytes should be mentioned: magnesium organochloro aluminate compounds, boron based electrolytes and a mixture of the Hauser base HMDSMgCl (hexamethyldisilazide magnesium chloride) and the Lewis acid AlCl_3 .

Magnesium organohaloaluminate electrolytes consist of ethereal solvents and complexes of the $\text{Mg}(\text{AlCl}_{4-n}\text{R}_n)_2$ type [30]. The electrolyte APC (a solution of 0.5 M PhMgCl and 0.25 M AlCl_3 in THF), as an example, shows anodic limits up to 3.3 V (vs. Mg/Mg^{2+}) and complete reversibility [31]. A transmetallation reaction between $\text{R}_x\text{MgCl}_{2-x}$ and $\text{R}'_y\text{AlCl}_{3-y}$ results in the formation of these complexes. The particular equilibrium species are determined by various factors like the acid/base ratio, temperature, solvent, concentration and the specific organic groups. Studies of these electrolytes support following conclusions [30]:

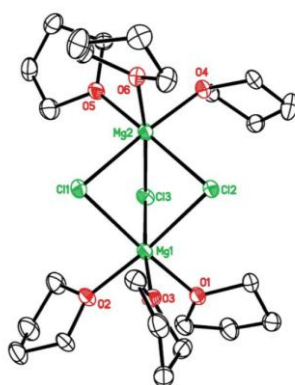


Fig. 2 ORTEP plot of $[\text{Mg}_2(\mu - \text{Cl})_3 \cdot 6\text{THF}]^+$ [32].

- Mg_2Cl_3^+ is the main electroactive ionic species that allows reversible Mg plating (Fig. 2)

- The anodic stability of the electrolyte is higher if the Cl:R ratio is large at a constant Al:Mg ratio. However, more organic ligands have a positive effect on electro-deposition overpotential and the cycling efficiency.
- The anodic stability is further improved if aliphatic ligands are replaced by aryl groups such as phenyl, because in this case β -H elimination is prevented as possible oxidation process.
- Ionic conductivity depends on the Al:Mg ratio, the organic ligands and the concentration. The more different anionic species are present in the solvent the higher the ionic conductivity.

In **boron based electrolytes** [33] different boron molecules such as trixylylborane or tris(pentafluorophenyl)borane instead of aluminum compounds are mixed with Grignard reagents. So far $B(C_6F_5)_3$ -PhMgCl exhibits the largest electrochemical potential window (3.7 V vs. Mg/Mg²⁺) [32]. The synthesis and characterization of this electrolyte was part of this diploma thesis.

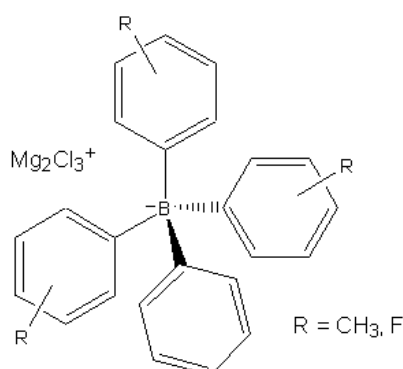


Fig. 3. Boron complex with different aryl groups.

The third electrolyte of this kind **HMDSMgCl-AlCl₃** has been studied as a possible electrolyte in Mg-S batteries [32]. Since sulfur readily reacts with nucleophilic components like Grignard reagents, those are substituted by a Hauser base. This electrolyte showed excellent reversibility for Mg deposition and stripping and an anodic stability of 3.2 V (vs. Mg/Mg²⁺). The first cycling experiments with a Mg anode and a sulfur cathode showed promising results in the first cycle, but the discharge capacity faded in further cycles due to the formation of polysulfides or sulfur dissolution [20].

Other than the previous mentioned electrolytes, there are non-Grignard based ones as well. Non-nucleophilic **MgCl₂ can be mixed with different Al-based Lewis acids** (AlCl₃, AlPh₃, AlEtCl₂) in a very convenient way to generate Mg²⁺ conductive electrolytes [34]. They exhibit nearly full reversibility and anodic stabilities up to 3.4 V (vs. Mg/Mg²⁺). The ionic conductivities vary from 0.3·10⁻³ mS/cm for MgCl₂-AlCl₃ to 7·10⁻³ mS/cm for MgCl₂-EtAlCl₂. The low conductivity of the first electrolyte is caused by the low solubility of MgCl₂

in the AlCl_3/THF solution. But still these electrolytes seem to be promising for battery applications and have also been investigated by other research groups [35].

Finally, another **electrolyte comprising ROMgCl and AlCl_3** should be mentioned. Their advantage is their air stability and moderate anodic stability of approx. 2.6 V (vs. Mg/Mg^{2+}) [36].

1.2.4.2 Ionic liquid based electrolytes

Electrodeposition from **ionic liquids** has also been reported [37,38]. The Mg-ion source was $\text{Mg}(\text{CF}_3\text{SO}_3)_2$ dissolved in different ionic liquids (e.g. $[\text{BMIM}]\text{BF}_4$). However, other researchers [39] including ourselves could not achieve any reversible Mg deposition out of this ionic liquid. Like the other author, we had difficulties to dissolve the $\text{Mg}(\text{CF}_3\text{SO}_3)_2$ in the mentioned water-free ionic liquid. A different approach was using a Grignard reagent as Mg source instead of a magnesium salt which was dissolved it in a binary ionic liquid system [40].

1.2.4.3 Polymer based electrolytes

In contrast to batteries build with liquid electrolytes, a completely solid state Mg-ion battery would have some benefits: flexibility in geometry, no electrolyte leakage and no safety issues due to possible short circuits. Similarly to Li-polymer batteries, there have also been attempts to find electrolytes for the solid state magnesium battery [18].

In general a **polymer based electrolyte** consists of a Mg-salt dissolved in a polymer matrix. The problem of this “solid polymer electrolyte” is the low conductivity of the Mg-ion in the polymer matrix. To enhance ionic conductivity “gel-polymer-electrolytes” are more favorable [18]. Those include plasticizers and nano-particles for improved ionic conductivity and mechanical stability.

By now there are only few reported electrolytes. Mainly salts like $\text{Mg}(\text{ClO}_4)_2$, MgCl_2 , $\text{Mg}(\text{CF}_3\text{SO}_3)_2$ and $\text{Mg}(\text{TFSI})_2$ are dissolved in polymer matrices like PEO or PVdF. Plasticizers are mostly ethereal solvents or ionic liquids. The crucial factors for polymer and other electrolytes are:

- high transfer number of Mg-ions
- mechanical stability
- compatibility with electrodes
- high ionic conductivity

Table 4 summarizes the proposed systems for polymer based and ionic liquid based electrolytes:

Table 4 Properties of current investigated polymer electrolytes [18].

Salt	Polymer	Plasticizer	Fillers	Property	Reference
Polymer based electrolytes					
Mg(ClO ₄) ₂ or MgCl ₂	PEO				[41,42]
EtMgBr	PEO	THF		$\sigma = 10^{-4}$ - 10^{-5} mS cm ⁻¹ (T=50°C), reversibility of Mg deposition due to EtMgBr	[43]
Amidomagnesiumchlorides	PEO	THF			[44]
MgTf ₂	PEO, PAN, PVDF or PMMA	PC, EC		poor cycling properties, low mechanical strength	[45-48]
Mg(CF ₃ SO ₃) ₂	PVDF	TG	TBACl	$\sigma = 5 \cdot 10^{-4}$ mS cm ⁻¹ ; anodic limit 1.75 V	[49]
Mg(CF ₃ SO ₃) ₂ or Mg(TFSI) ₂	PEO-PMA	EMITFSI or DEMETFSI		$\sigma = 3.5 \cdot 10^{-3}$ mS cm ⁻¹ (80wt% EMITFSI and 20mol% Mg(TFSI) ₂)	[50]
Mg(ClO ₄) ₂	PVdF-coHFP	EC/PC	SiO ₂	poor cycling properties, high overvoltage	[51]
Mg(ClO ₄) ₂	Acetamide			amorphization of MnO ₂ cathode lead to poor cycling	[52]
Ionic liquid based electrolytes					
MeMgBr		DEME ⁺ (TFSI ⁻)(FSI ⁻)		90% CE for about 100 cycles	[40]
Mg(CF ₃ SO ₃) ₂		BMIMPF ₄			[37]

2 Methods

2.1 Multinuclear NMR

Modern NMR techniques allow to measure nuclei other than ^{13}C or ^1H . Since these techniques are mainly used by specialized researchers in this area, an overview of the differences of hetero-nuclei compared to ^1H and ^{13}C should be outlined here. It is limited to ^{11}B , ^{27}Al and ^{19}F NMR, because those are the nuclei investigated in this master thesis.

NMR active nuclei can be divided into two main classes: Nuclei with spin $I = 1/2$ (e.g. ^1H and ^{19}F) and nuclei $I > 1/2$ (e.g. ^{11}B and ^{27}Al). While the first ones show sharp resonance lines, nuclei like ^{11}B or ^{27}Al show broad lines due to a very short spin-lattice relaxation time. This fact often impedes the identification of signals. Background signals are a common problem coming from the probehead or in the case of ^{11}B from the NMR tubes. Most of them are made out of borosilicate glasses. Therefore, often a blank test is required. At the same hetero-nuclei depend stronger on concentration, temperature and the used solvent, hence it is not unusual that chemical shifts vary by several ppm [53].

2.1.1 ^{11}B Boron

Boron possesses two NMR active nuclei ^{10}B and ^{11}B , both having a quadrupole moment ($I > 1/2$) [54]. More commonly used is ^{11}B because it offers some benefits over ^{10}B . It is more naturally abundant (80.4 % vs. 19.6 %) and has a smaller quadrupole moment ($3/2$ vs. 3). Thus, ^{11}B leads to more intense and sharper resonance lines. The differences compared to ^1H are in particular the larger chemical shifts, the coupling constants of {B-B}, which normally cannot be observed due to the large peak half width, and the coupling between a proton and the boron nucleus is resulting in a 1:1 doublet in the boron spectra. This effect is due to the orientation of the H-atom in the magnetic field – it can be either antiparallel or parallel orientated. This information is relevant for boron hydrides, however most spectra are proton decoupled. Hence, only singlets are observed. Proton decoupling is done, because primarily the coordination number of the boron atom needs to be identified. Tricoordinated boranes can be found with chemical shifts between 92 ppm – -8 ppm while the addition of another ligand shifts the borate anions upfield (+28 – -126 ppm) [55]. Fig. 4 summarizes the shifts for different boron compounds. They are given relative to $\text{BF}_3 \cdot \text{OEt}_2$ which is nowadays used as standard reference. The chemical shift of tetracoordinated boron atoms has not only a dependency on the solvent and concentration but also on the cation present in solution [56].

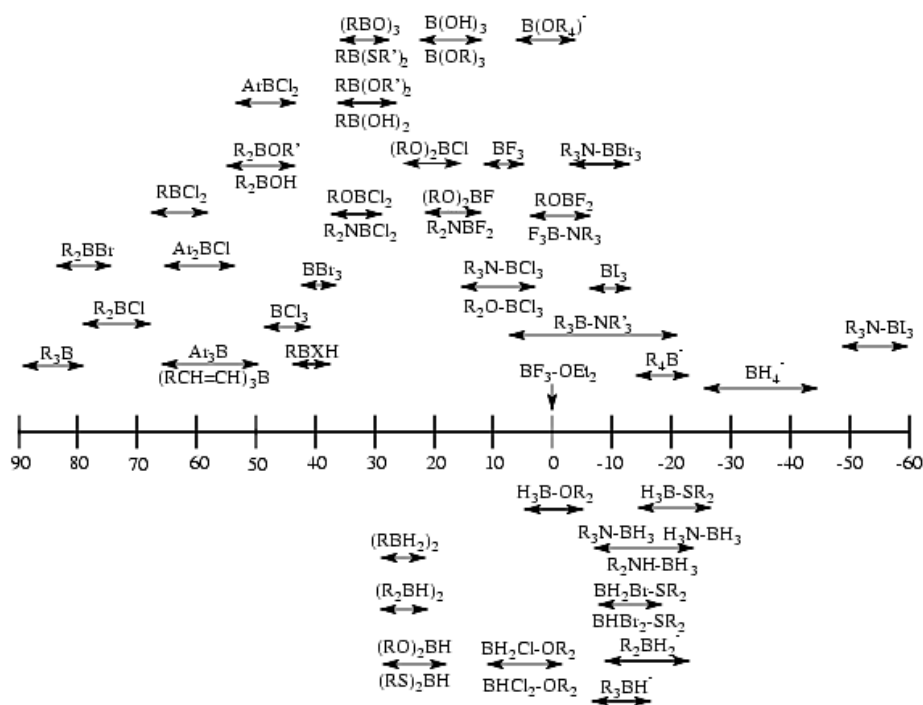


Fig. 4 Shifts of ^{11}B molecules relative to $\text{BF}_3\cdot\text{OEt}_2$ [56].

2.1.2 $^{27}\text{Aluminum}$

$^{27}\text{Aluminum}$ has a natural abundance of 100 %, which favors a reasonable spectral intensity, however, the quadrupole moment is higher than for boron, namely $I = 5/2$. This causes even broader lines (2 Hz – 60 kHz) and therefore the resonance lines often overlap. The linewidth is influenced by temperature, concentration and the pH value in aqueous solution. The shifts are commonly referred to $\text{Al}(\text{H}_2\text{O})_6^{3+}$ because of its narrow linewidth about 2 Hz and its easy preparation but other external reference such as $\text{Al}(\text{acac})_3$ have been reported in literature as well [53]. The main purpose of ^{27}Al NMR is the identification of the bound ligands and the nature of the formed species. The shifts in aluminum NMR reflect the coordination number which strongly depends on the used solvent. In aqueous solutions the aluminum compound is present as tri- or six-fold coordinated complex. In other solvents (e.g. methyl cyanide – weak solvent) AlCl_3 , as an example, can dimerize and exists in its octahedral state. So called strong solvents are able to dissociate the AlCl_3 dimer and give a resonance line in the tetracoordinated region. Even 5-fold coordinated species exist. Like for the ^{11}B NMR the anion shift can slightly depend the cation [57].

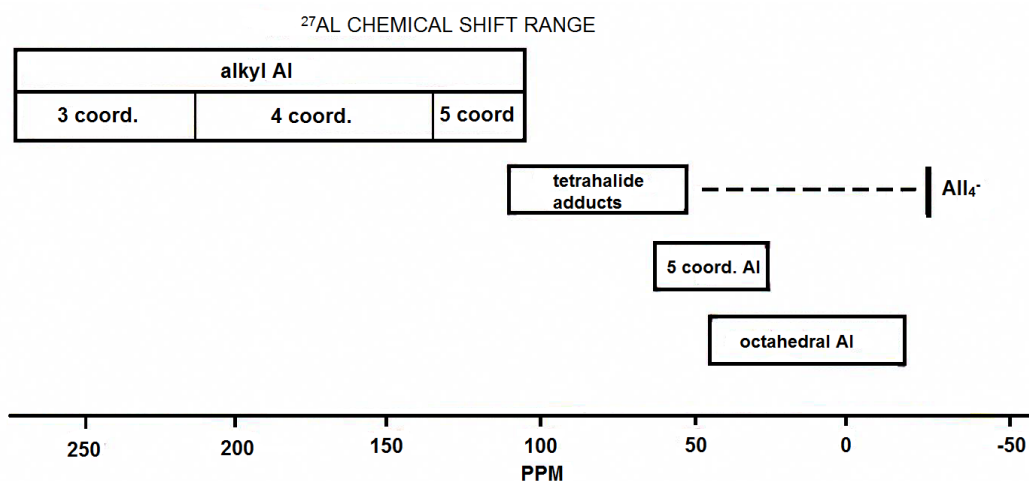


Fig. 5. Shifts of different coordinated aluminum compounds (ref. $\text{Al}(\text{H}_2\text{O})_6^{3+}$) [57].

2.1.3 ¹⁹Fluorine

Fluorine NMR is quite similar to ¹H. The spin number of ¹⁹F NMR equals $I = 1/2$ and it is the only isotope occurring in nature. It is routinely used to identify organic and organometallic compounds. In contrast to ¹H-NMR, ¹⁹F-NMR reveals a wider range of chemical shifts (about 500 ppm) and the homo-coupling of fluorine atoms is much larger. In addition, the used solvent has more impact on the chemical shift of ¹⁹F-NMR – they can differ up to 5 ppm. Moreover, fluorine NMR spectra nearly do not show any overlapping of signals and for the measurement no deuterated solvent is needed [58]. Another advantage is that signal intensities correlate with the accurate number of fluorine atoms. Most commonly CF_3Cl ($\delta = 0$ ppm) is used as reference substance.

NMR of fluoroaryl groups

Most fluorine spectra show spin-spin coupling of first order, so the spin-spin coupling multiplicities follow the $n+1$ rule. However, fluoroaryl components with more than one fluorine atom are of second order and therefore often difficult to interpret. The shifts of pentafluorophenyl groups normally follow this order: $\delta_{\text{ortho}} > \delta_{\text{para}} > \delta_{\text{meta}}$. They can vary considerably depending on the particular pentafluorophenyl derivate [59].

2.2 Electrochemical methods

2.2.1 Cyclic voltammetry

In cyclic voltammetry (CV) the potential of the working electrode with respect to the reference electrode is changed linearly with time and the resulting current flowing through the working electrode is measured. The $E(t)$ curve shows a triangular wave function (Fig. 6a): Starting at a particular value E_{st} the potential is changed with a constant velocity (scan rate) and after reaching a switching potential E_{λ} it is swept back to the starting potential. Depending on the applied potential, different redox reactions occur at the electrode/electrolyte interface which cause the measured current. The resulting cyclic

voltammogram (i vs. E) is basically determined by 2 factors: mass transport and charge-transfer.

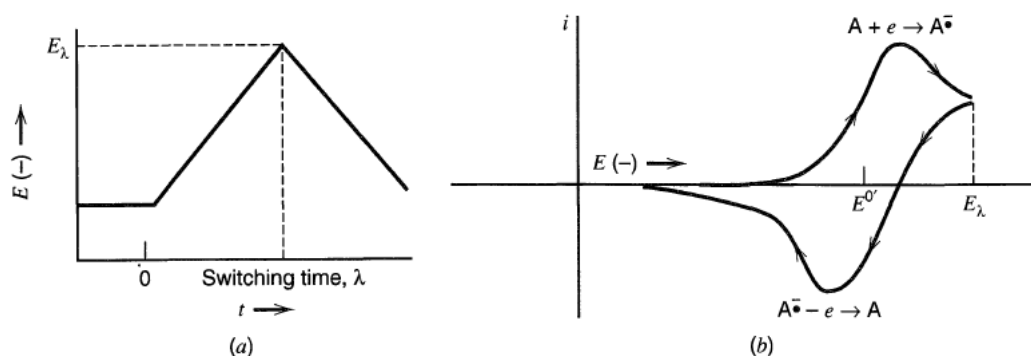


Fig. 6 Triangular potential wave function (a), cyclic voltammogram (b) [60].

2.2.2 Chronoamperometry

In chronoamperometry a leap from the open circuit potential to a potential which causes a faradaic current is applied (Fig. 7a). This current flows because instantly a reduction or oxidation of the electroactive species takes place. Due to this reaction a concentration gradient results on the working electrode and causes a flux towards the surface. The current can be described by the Cottrell equation (formula (13) p. 31) if the electrode reaction is limited by diffusion.

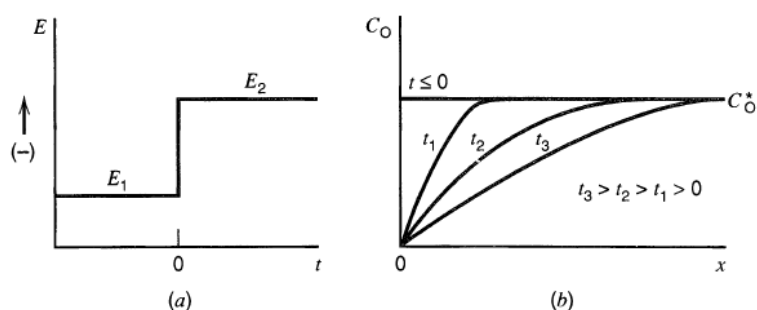


Fig. 7 Potential step (a), concentration gradient over time (b) [60].

3 Objective

Concerning magnesium based secondary batteries research is still in a nascent stage compared to Li/Li-ion batteries. The challenge is to find a system which allows reversible Mg cyclization between anode and cathode. This requires a passive layer free anode, fast intercalation of Mg-ions in the cathode material and fast diffusion of the bivalent ion in the electrolyte. But the sluggish transport of bivalent ions in solid frameworks and electrolytes is still an unexplained phenomenon. There is a great demand to find explanations, which can help to develop highly conductive, electrochemical stable and non corrosive electrolytes.

The main goal of this master thesis is to identify electrolytes which exhibit coulombic efficiencies >90 % for the Mg deposition/dissolution reaction and anodic stabilities >3 V (vs. Mg/Mg²⁺). For the preparation of magnesium-organoborate electrolytes, commercially non available triarylboranes have to be synthesized and the reaction products will be analyzed by ¹¹B-NMR and HPLC. One magnesium-organoborate electrolyte (B(C₆F₅)₃-PhMgCl), two other electrolytes (all phenyl complex and magnesium aluminum chloride complex) and the Grignard solution phenylmagnesium chloride in THF (part of two electrolytes) will be investigated by cyclic voltammetry and chronoamperometry to gain information on the reversibility of Mg deposition/dissolution and thermodynamic parameters. Static and rotating platinum and glassy carbon disk electrodes will be used. For understanding the electrode reactions in these electrolytes, the identity of different species in the electrolytes will be characterized employing multinuclear NMR-spectroscopy.

Since a battery basically consists of an anode, electrolyte and a cathode, it is of peculiar interest to examine the cyclization of anode- and cathode materials in a suitable electrolyte. Low alloyed magnesium metals will be used as anode materials. These anodes will be cyclized and compared to pure magnesium (99.9 %).

4 Experimental part

4.1 Chemicals and materials

4.1.1 Chemicals

Table 5: Chemicals

Chemical	Supplier
1-Bromo-3,5-dimethylbenzene 97 %	Sigma-Aldrich, Vienna, Austria
2-Butanol anhydrous, 99.5 %	Sigma-Aldrich, Vienna, Austria
4-Phenylazodiphenylamine 97 %	Alfa Aesar, Karlsruhe, Germany
Aluminiumchloride anhydrous, PURATREM 99.99+ %	Strem chemicals Inc., Kehl Germany
Bis(cyclopentadienyl)cobalt(II) >98 %	abcr chemicals, Karlsruhe, Germany
Bis(cyclopentadienyl)iron	Neuber AG, Vienna, Austria
Boron trifluoride Diethyl etherate purified by redistillation >46.5 %	Sigma-Aldrich, Vienna, Austria
Bromobenzene reagent plus® 99 %	Sigma-Aldrich, Vienna, Austria
Chloroform D ≥99.8 %	Eurisotop, Saarbücken, Germany
Diethylether anhydrous	Institute of inorganic chemistry, TU Graz
Magnesium turnings, reagent grade 98 %	Sigma-Aldrich, Vienna, Austria
Magnesiumchloride ultra dry, 99.99 %	Alfa Aesar, Karlsruhe, Germany
Methylenchloride D2 ≥99.6 %	Eurisotop, Saarbücken, Germany
Penatfluorophenyl magnesiumbromide 0.5 M in diethylether	Sigma-Aldrich, Vienna, Austria
Phenylmagnesium chloride 2 M in THF	Sigma-Aldrich, Vienna, Austria
Tetrahydrofuran anhydrous, >99.9 %, inhibitor free	Sigma-Aldrich, Vienna, Austria
Toluene anhydrous	Institute of inorganic chemistry, TU Graz
Trimethyl borate purified by redistillation >99.5 %	Sigma-Aldrich, Vienna, Austria
Tris(pentafluorophenyl)borane	Boulder Scientific Company, Colorado USA

4.1.2 Anode materials

The magnesium alloys were received from Leichtmetallkompetenzzentrum Ranshofen GmbH (LKR). Mg 99.9 % was purchased from Goodfellow, Bad Nauheim, Germany.

Table 6: Elemental composition of the magnesium anode alloys.

Element	MgGd	MgGdZn	Mg 99.9 %
Mg	98.57	98.54	99.94
Mn	0.00	0.00	0.0170
Fe	0.02	0.03	0.0280
Zn	0.00	0.95	0.0020
Gd	1.42	0.48	-
Si	-	-	0.0050
Al	-	-	0.0070

4.1.3 Equipment

Potentiostat

Autolab PGSTAT 100: Metrohm Autolab B.V., Utrecht, Netherlands

Software Nova 1.10: Metrohm Autolab B.V., Utrecht, Netherlands

Polishing machine

Struers, LaboSystem (LaboPol-25, LaboForce-3), Willich, Germany

Karl-Fischer-Titration

CA-100/VA-100, Mitsubishi Chemicals Corp., Tokyo, Japan

Schlenk line (max. vacuum: 9×10^{-3} mbar)

Schlenk line: custom-built model, grease free without ground joints, Bartelt, Graz, Austria

Rotary vane pump, DUO 5 M, Pfeiffer Vacuum, Asslar, Germany

Glovebox

MB G-120, MBraun, Garching, Germany

GC/MS

Gas chromatograph: Agilent Technologies 7890A; Column: HP-5 30 m (length) x 0.25 mm (ID) x 0.32 μ m (film), Agilent

Mass spectrometer: Agilent Technologies 5975C inert MSD with a triple-axis detector

NMR

^{11}B , ^{27}Al , ^{19}F : Mercury 300 MHz Spectrometer, Varian

^{19}F : Inova 500 MHz Spectrometer, Varian

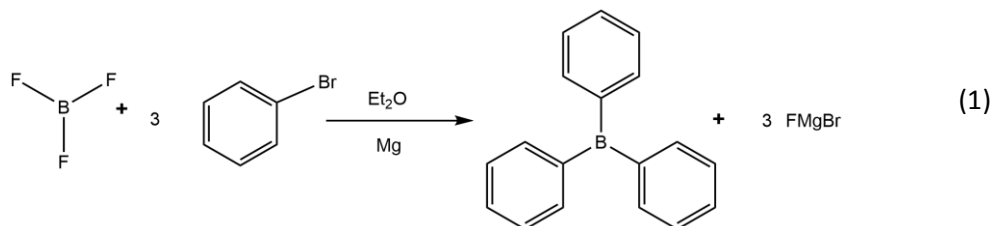
^{13}C : Ultrashield 300 MHz Spectrometer, Bruker
screw-mountable NMR tubes

HPLC

Agilent 1100 Series HPLC; Column: Phenomenex Kinetex XB-C18 50x2.1 mm 2.6 μ m 100A

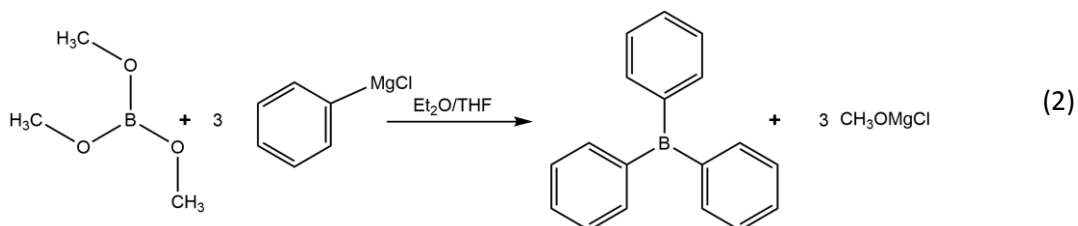
4.2 Synthesis

4.2.1 Triphenylborane - Halide approach

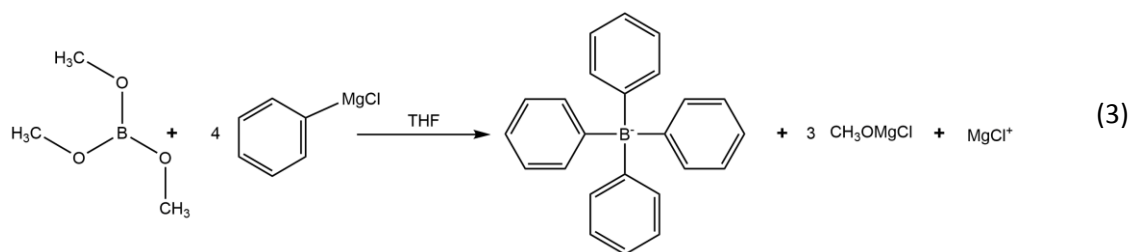


Triphenyl borane (equation (1)) was synthesized according to Brown *et al.* [61]. A flamed dried 50 ml three-neck reaction flask, equipped with a reflux condenser and a dropping funnel was charged with Mg turnings (40 mmol) and one crystal of iodine. 15 ml of anhydrous ether were added under dry N_2 atmosphere. While stirring the solution the reaction was initiated by the dropwise addition of bromobenzene (35 mmol) in 10 ml of ether. If the reaction did not start immediately (indicated by refluxing of the ether) the mixture was heated. The solution was stirred for half an hour and then the $\text{BF}_3 \cdot \text{OEt}_2$ (10 mmol) was added. Shortly after the addition a white precipitate formed. The course of the reaction was followed by ^{11}B NMR.

4.2.2 Triphenylborane - Grignard approach



For the second approach a commercially available 2 M phenylmagnesium chloride solution was reacted with either trimethyl borate or borontrifluoride diethyletherate (equation (2)). The Grignard solution was titrated prior to use according to the procedure described in 4.3.1.3. 1 ml (2.1 M) of the Grignard solution was added dropwise under inert conditions to a Schlenk flask containing 0.7 mmol of trimethyl borate (or borontrifluoride diethyletherate) in 1.0 ml of anhydrous ether. During the reaction with borontrifluoride diethyletherate, the formation of precipitates was observed, whereas for the reaction with trimethyl borate the solution remained clear. The reaction progress was monitored by ^{11}B NMR.



This approach was slightly modified. Instead of a molar ratio of 1:3 (trimethyl borate: PhMgCl) the reaction has been performed with a ratio of 1:4 to directly synthesize the boron complex (equation (3)). The procedure is described in the previous paragraph.

4.2.3 HPLC

For HPLC analysis 10 μl samples of the reaction mixture were diluted with 1000 μl of THF in 1.5 ml amber glass vials.

For a 1.0 mg/ml standard solution, 52.4 mg of sodium tetrakisphenyl borate (TPB) were diluted with water. This stock solution was later on diluted with THF in amber glass vials to a concentration of 100 $\mu\text{g/ml}$. The parameters for HPLC analysis are summarized in Table 7.

Table 7: Method for the separation of synthesis constituents in TPBA synthesis solution.

Parameter	Value	
Flow (ml/min):	0.25	
Mobile phase:	A: 0.1 % NH_4COOH (ammonium formate) B: acetonitrile	
Injection volume (μl):	2	
DAD wave length (nm):	240	
Autosampler temp. ($^\circ\text{C}$):	15	
Column temp. ($^\circ\text{C}$):	40	
Gradient:	Time (min)	%B
	0	20
	7	100
	12	100
	12.1	20
	20	20

4.2.4 GC/MS analysis

The GC analysis measurements were carried out with helium 5.0 as mobile phase and the column temperature program was as follows: 1 min at 50°C , then the column is heated 40°C/min to 300°C and this temperature is kept for 5 min.

4.3 Electrolyte preparation

4.3.1 General

4.3.1.1 Degassing of solvents

For removing dissolved gases a flame dried Schlenk-flask was filled with an anhydrous solvent (e.g. THF, toluene) and connected to a vacuum line. The solvent was cooled down to -196°C by liquid nitrogen and was kept at this temperature for 15 minutes until it was completely frozen. Now vacuum was applied for at least 15 minutes to degas the flask. The Schlenk-flask was disconnected from the line and the solvent was brought to room temperature again. This freeze-pump-thaw procedure was repeated 3 times.

4.3.1.2 Water content determination

For all syntheses and electrolyte preparations the water content of the used solvent was determined by Karl-Fischer titration. This method is based on the oxidation of sulfur dioxide by iodine in the presence of water. For each measurement 1.0 ml of the solvent was injected into the Karl-Fischer device (CA-100/VA-100, Mitsubishi Chemicals Corp., Tokyo, Japan) and weighed before and after the titration in order to determine the ppm content of water.

4.3.1.3 Titration of Grignard solutions

A 0.99 M stock solution can be prepared by addition of 10.0 ml of 2-butanol to 100.0 ml of absolute, degassed toluene in a complete dry glass jar. This stock solution is stored under an atmosphere of dry argon over 3 Å molecular sieves (this solution is stable for several months).

For titration 2-5 mg of 4-phenylazodiphenylamine were dissolved in 1.0 ml of stock solution. While stirring the stock solution, the Grignard reagent was added dropwise by a syringe till the solution showed a color change from yellow to pink. The titration was carried out at least 3 times to get a reliable result [62].

4.3.2 PhMgCl

For electrochemical measurements, 1 M of PhMgCl in THF were obtained by dilution of a commercial 2 M solution of PhMgCl in THF.

4.3.3 1:2 all phenyl complex (APC)

Although the commercial THF was anhydrous (Sigma-Aldrich <20 ppm), it was firstly dried for 24 h with 3 Å molecular sieves to reach a water content below 10 ppm.

For preparation of the APC solution, a required amount of anhydrous AlCl_3 (1 mole equivalent) was slowly poured to vigorously stirred THF. Two mole equivalents of phenylmagnesium chloride in THF (the molarity of the solution was determined by

titrimetric analysis described in 4.3.1.3) were added dropwise to the solution containing AlCl_3 . The electrolyte was stirred for 16 hours [63].

4.3.4 BCF-PhMgCl electrolyte

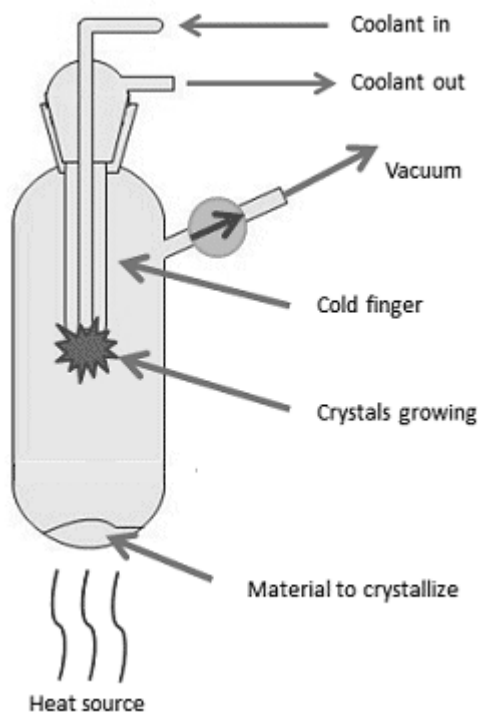


Fig. 8 Vacuum sublimation apparatus [75].

Tris(pentafluorophenyl) borane (used as received) was dissolved in anhydrous THF (<10 ppm of water). PhMgCl was added to this brown-yellowish colored solution under stirring. For the electrochemical experiments, solutions containing 0.2 M of BCF with different molar ratios of PhMgCl were prepared, namely 1:3, 1:2 and 1:1 $\text{B}(\text{C}_6\text{F}_5)_3$:PhMgCl. Therefore, 0.6 M, 0.4 M and 0.2 M of PhMgCl was added to the solution.

An attempt to remove impurities from BCF was made by vacuum sublimation. $\text{B}(\text{C}_6\text{F}_5)_3$ was transferred into a Schlenk flask under inert conditions. The flask was closed with a cooling finger and sealed. After connecting the flask to a vacuum line and applying a pressure of $3 \cdot 10^{-2}$ mbar, BCF was heated to 80°C to start the sublimation. This temperature was kept for 20 h and then the flask with the cooling finger was transferred

into the glovebox. Therefore, the outer part of the cooling finger needed to be dried of any water traces by compressed air. The sublimated crystals on the cooling finger were collected and analyzed by ^{19}F NMR.

4.3.5 Saturated magnesium aluminum chloride complex (MACC)

For this electrolyte AlCl_3 and MgCl_2 (both reagents were used as received) were dissolved in a 1:2 molar ratio in THF [35]. To a suspension of freshly ground MgCl_2 in THF (anhydrous MgCl_2 has a poor solubility in THF¹) a solution of AlCl_3 in the same solvent was added dropwise with a syringe. After stirring over night white particles were still visible. Therefore the solids were allowed to settle and the supernatant yellowish fluid was collected by a syringe and used as electrolyte.

¹ Heating to ≤ 30 degrees Celsius made nearly no difference

4.4 Electrolyte characterization

4.4.1 Cyclic voltammetry and chronoamperometry

For the characterization by means of cyclic voltammetry, parameters like the scan rate, potential window (anodic/cathodic limit) and electrode materials were varied (platinum or glassy carbon electrode).

In chronoamperometry the working electrode potential was kept at the OCP for 30 s and the step potential was varied and held for 120 s.

All cyclic voltammetry and chronoamperometry experiments were carried out at the same temperature (30°C) and in argon atmosphere. While the stirring needed to be turned off during the measurement, the solution was stirred in between for at least 30 seconds. The experimental data was analyzed by NOVA 1.10 software and plotted in Origin 9.0 software.

4.4.1.1 Cell and electrodes setup

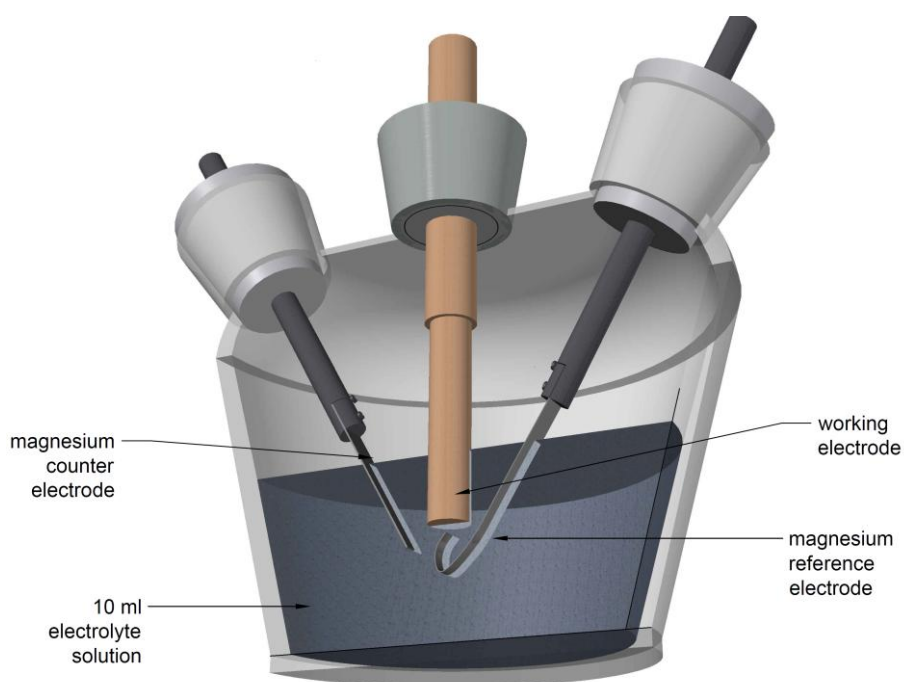


Fig. 9. Measurement cell for electrolyte characterization.

Electrochemical cells with 3-electrode arrangement filled with 10 ml electrolyte solution were used in all experiments. The setup was arranged in an argon filled glovebox and inside a faraday cage in order to record the data with a good signal to noise ratio. Three ground joints of the cell were needed for the electrodes while the additional two joints were sealed to prevent the evaporation of the solution (b.p. THF 66°C). For the measurements different **working electrodes** were used:

- a. The electrochemical characterization of different electrolytes was carried out using 3 mm diameter glassy carbon and platinum disk electrodes (rotating and static, Metrohm). The electrodes were polished according to the procedure described in 4.4.1.2. if needed.
- b. For the characterization of magnesium alloys and pure magnesium these materials were used as working electrodes. The electrodes were punched out of the alloy foil (less than 300 μm thick) and ground with SiC sandpaper (1200-4000 mesh) outside the glovebox. Another grinding step with 4000 mesh SiC grit-paper was performed in argon atmosphere to remove the MgO layer. Fig. 10 shows a sketch of the electrodes. The disk had a diameter of 10 mm and was dipped into the solution.



Fig. 10. Mg-alloy electrode disk diameter $d = 10$ mm.

Unless indicated otherwise, a magnesium foil (Goodfellow 99.9 %) was applied as **reference and counter electrode**. The electrode foils were ground with 1200 mesh SiC paper and washed with dry THF in the glovebox in order to remove the passive film.

4.4.1.2 Polishing the electrodes

The working electrodes were ground and polished prior to the measurements if scratches were obvious. With 800 mesh SiC grit-paper the electrode was flattened and then ground step by step with 1200, 2400 and 4000 mesh SiC paper. Each step was done for 2 minutes at a rotation speed of 250 rpm.

The polishing of the electrodes was carried out in two steps: firstly on a MD-Chem polishing disc with DP-suspension 3 μm as abrasive and DP-lubricant red. Secondly, on a MD-Mol polishing disc with OP-Suspension 0.04 μm as abrasive and lubricant. Each polishing step lasted 4 min at a rotation speed of 150 rpm.

4.4.2 NMR

For the speciation of the electrolytes, NMR spectra of ^{11}B (96.3 MHz), ^{19}F (282 and 470 MHz), ^{27}Al (78.2 MHz), ^{13}C and ^1H nuclei were recorded in anhydrous THF with a D_2O capillary for the external lock signal. Investigations of $\text{B}(\text{C}_6\text{F}_5)_3$ were done in anhydrous CD_2Cl_2 or CD_3Cl solvent (stored over molecular sieves). The chemical shifts are given in ppm relative to $\text{BF}_3 \cdot \text{Et}_2\text{O}$ for ^{11}B , CFCl_3 for ^{19}F and $\text{Al}(\text{H}_2\text{O})_6^{3+}$ for ^{27}Al spectra. The NMR tubes were flame dried and the samples were filled under inert conditions either in the glovebox or in a Schlenk flask in a dry N_2 counter-flow arrangement.

Furthermore, ^{11}B NMR was used to follow the reaction progress in triphenyl borane or trixylyl borane synthesis and for examination of the products.

5 Results and discussion

5.1 Synthesis

5.1.1 Halide approach

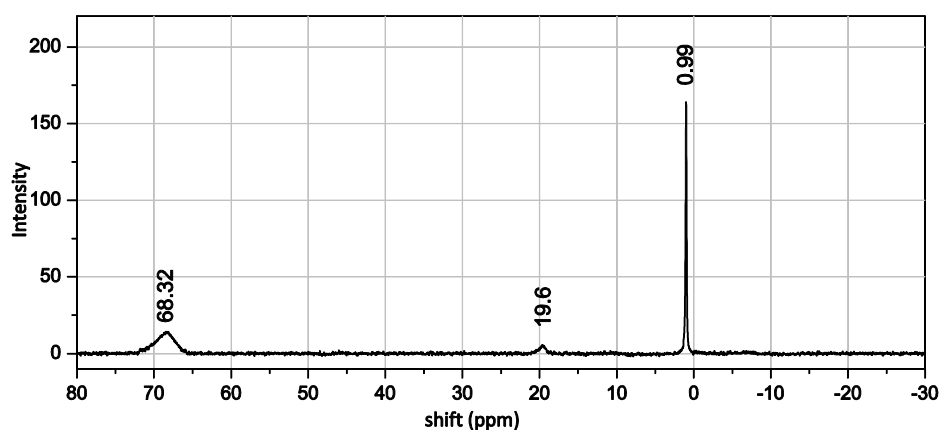


Fig. 11. ^{11}B NMR spectrum of the halide approach at 96.3 MHz, 25°C, external lock signal: D_2O .

A ^{11}B -NMR was recorded of the reaction mixture (Fig. 11). It showed a resonance line at $\delta = 1.0$ ppm and a broad resonance at $\delta = 68.3$ ppm. The latter resonance signal can be assigned to triphenyl borane. The high narrow peak might be unreacted borontrifluoride diethyletherate because the whole spectrum seems to be downfield shifted by approx. 1 ppm. At $\delta = 19.6$ ppm a very small signal is indicated which can be assigned to boronic acid. It forms if traces of water are present.

Of the same reaction mixture a GC/MS analysis was performed. It could only be used to determine side products of the reaction mixture since the sample needed to be diluted with methanol for the measurement. Methanol slowly causes alcoholysis of triphenylborane. GC/MS identified two main side products: biphenyl due to Wurtz coupling and unreacted bromobenzene.

Although we obtained the desired product in this approach further processing seemed to be useless because of the insufficient yield and the detected Wurtz coupling side product in GC/MS.

5.1.2 Grignard approach

5.1.2.1 Trimethyl borate adduct

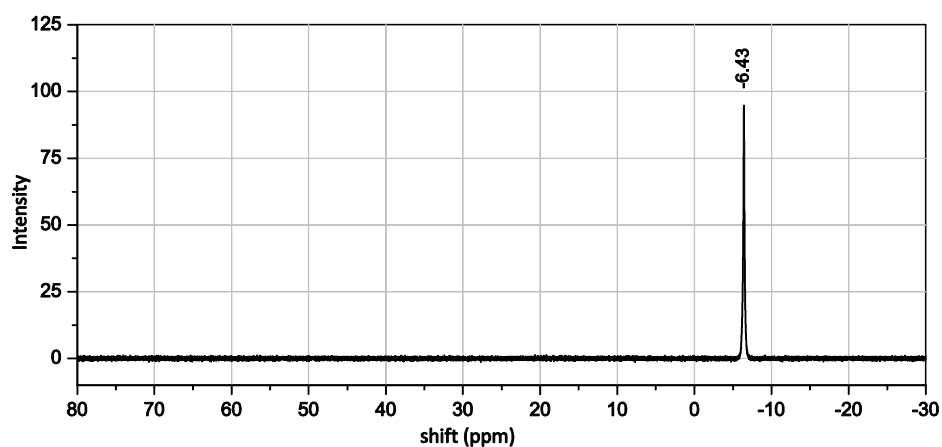


Fig. 12. ^{11}B NMR spectrum of the Grignard approach with trimethylborate adduct at 96.3 MHz, 25°C, external lock signal: D_2O .

Analyzing the 1:3 and the 1:4 mole ratio mixture of trimethylborate:PhMgCl solution by ^{11}B -NMR revealed only one quite sharp resonance line at $\delta = -6.43$ ppm (Fig. 12). This indicated the formation of a tetraphenyl borate anion (TPBA). Since the shift of tetra-coordinated boron species depends on the counter ion as well, this is an assumption based on the shifts of $\text{Na}[\text{BPh}_4]$ and $\text{K}[\text{BPh}_4]$ [64] – so mono valent cations. Likely, the counter ion in this solution is $[\text{Mg}_2\text{Cl}_3]^+$. Since the TPBA is not volatile enough for GC, the yield of TPBA was determined via HPLC analysis.

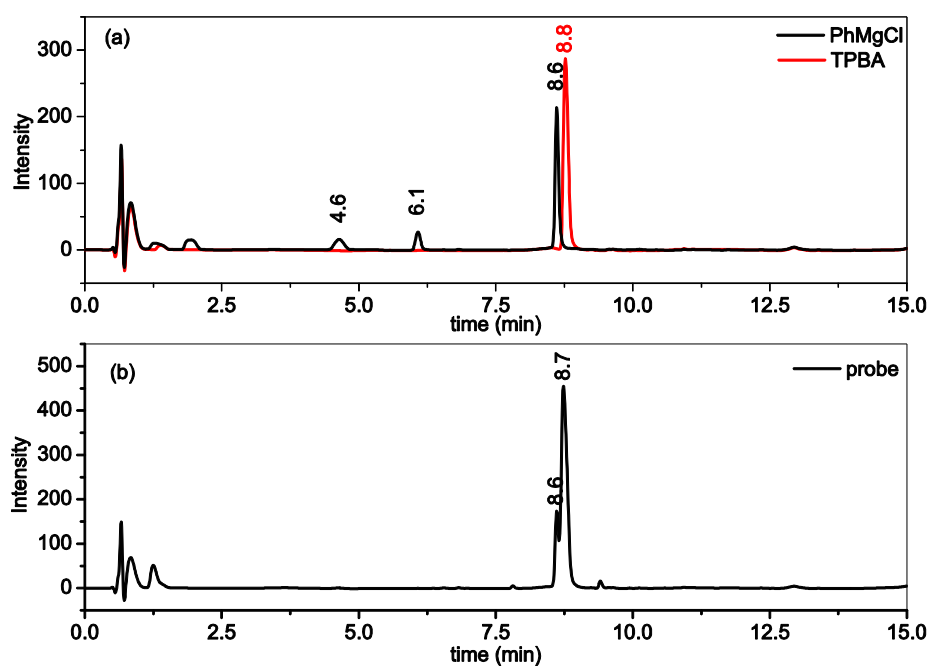


Fig. 13 HPLC analysis of the standard solution (a) and the electrolyte solution (b), prepared according to procedure 4.2.2 with trimethylborate.

The approach with one mole equivalent of trimethyl borate and four molar equivalents of PhMgCl should ensure a 100 % turnover to tetraphenyl borate. HPLC analysis of the reaction mixture (Fig. 13b) showed two main peaks at 8.6 and 8.7 min. Based on the standard solution (Fig. 13a) these peaks refer to PhMgCl (8.6 min) and TPBA (8.8 min). In the standard solution of PhMgCl two further smaller peaks at 4.8 and 6.1 min are monitored in the chromatogram. This is due to the Schlenk equilibrium of Grignard reagents. Three species namely PhMgCl, MgCl₂ and MgPh₂ are existent in THF.

The sample showed a significantly smaller turnover of tetraphenyl borate compared to the theoretical yield and remaining Grignard reagent. An exact integration of the peak areas was not possible since the two peaks overlap but an approximate peak area determination of the TPBA peak suggests a turnover of only 25 % compared to the theoretical yield. Further analysis will be needed to identify the discrepancy between the theoretical and measured yield of tetraphenylborate since no other boron compound was detected by ¹¹B-NMR.

It was not possible to use this solution for any electrolyte preparation because the required yield of tetraphenyl borate was not achieved. At the same time the turnover indicates a high yield of side products.

5.1.2.2 Borontrifluoride diethyletherate adduct

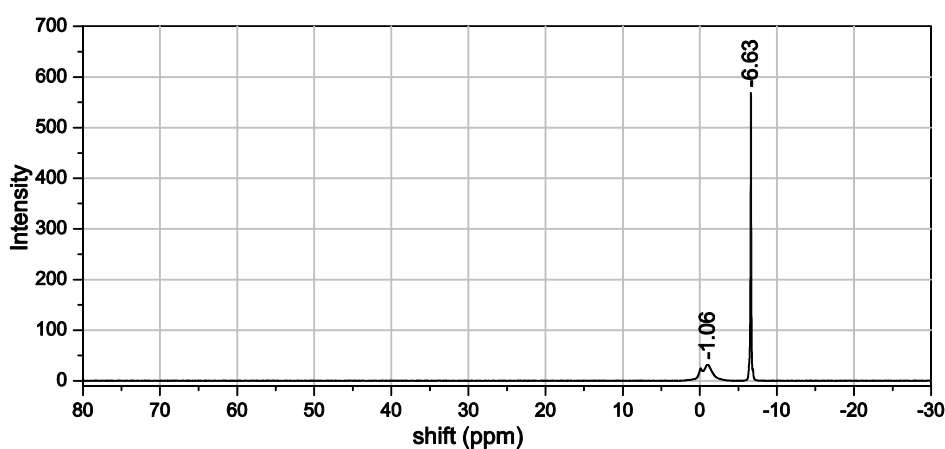


Fig. 14 ¹¹B NMR spectrum of the Grignard approach with BF₃ OEt₂ adduct at 96.3 MHz, 25°C, external lock signal: D₂O.

The same approach, using boron trifluoride instead of trimethylborate, produced even less satisfying results. The modification of the molar ratio (1:4) analyzed by ¹¹B-NMR revealed a resonance line for tetraphenylborate ($\delta = -6.63$ ppm) and a smaller signal at $\delta = -1.06$ ppm (Fig. 14) The HPLC showed a dominant signal at 7.6 min which could not be assigned and only small signals for remaining PhMgCl (8.6 min) and TPBA (8.8 min).

For the synthesis of pure triarylboranes or solutions containing triarylborate compounds further analysis with other methods than NMR or HPLC will be necessary to clearly identify the side products and to prevent their formation.

5.2 Electrolyte characterization

The characterization of the electrolytes was mainly done with electrochemical experiments to analyze their anodic stability and their reversibility for Mg deposition/dissolution. The current efficiency (equation (4)) of the metal deposition/dissolution reaction is defined as ratio of the anodic charge over the cathodic charge.

$$CE [\%] = \frac{Q_A}{Q_C} \cdot 100 \quad (4)$$

The difference of anodic and cathodic peak potentials is usually calculated to gain information on the electrochemical reversibility of an electrode reaction, but no real cathodic peak was obtained in most electrolytes, because the cathodic electrolyte decomposition interferes with the Mg deposition. Therefore, the difference between the dissolution peak potential and the interception point of the anodic trace with the zero current level is used as indicator for the reversibility.

Starting from the OCP, the potential was swept in negative direction unless indicated differently. To obtain an overview on the stability of the THF based electrolytes the typical potential range was between -0.5 V and 3.0 V which was scanned with $v = 50 \text{ mV s}^{-1}$. In literature, different cutoff criteria for electrolyte decomposition/electrochemical potential windows have been reported. For ionic liquids the cutoff current density equals generally 1.0 mA/cm^2 at a sweep rate of 50 mV/s in a linear sweep rate experiment [39]. For polymer electrolytes current density values of 0.05 mA/cm^2 at a scan rate of 1 mV/s in CV have been used [65]. For organic based electrolytes no general criterion exists and the cutoff potential values have been chosen quite arbitrarily. In this diploma thesis, the anodic stability voltage is measured at a current density value of 0.2 mA/cm^2 at 50 mV/s in CV. It is chosen lower than 1 mA/cm^2 to prevent overestimation of the actual anodic potential limit.

For the working electrode either platinum or glassy carbon were chosen. However, due to better current efficiencies obtained on the platinum electrode the measurements were mostly performed with this electrode. In Table 8 the results for cyclization experiments on Pt and GC electrodes for three different electrolytes are listed:

Table 8: Current efficiencies (CE) for 3 different electrolytes on Pt and GC electrodes.

Cycle	1 M PhMgCl		0.25 M APC 1:2		0.2 M BCF 1:3	
	CE(Pt) (%)	CE(GC) (%)	CE(Pt) (%)	CE(GC) (%)	CE(Pt) (%)	CE(GC) (%)
1	98.6	50.5	74.1	46.1	54.5	19.2
2	91.4	38.3	86.8	20.3	59.1	23.3
3	93.6	33.8	89.4	22.9	63.0	26.6

A significant difference between Pt and GC current efficiencies is obvious. While the current efficiency is constant or even rises with each cycle on Pt, the current efficiency on GC electrodes is far lower or even decreases during cyclization.

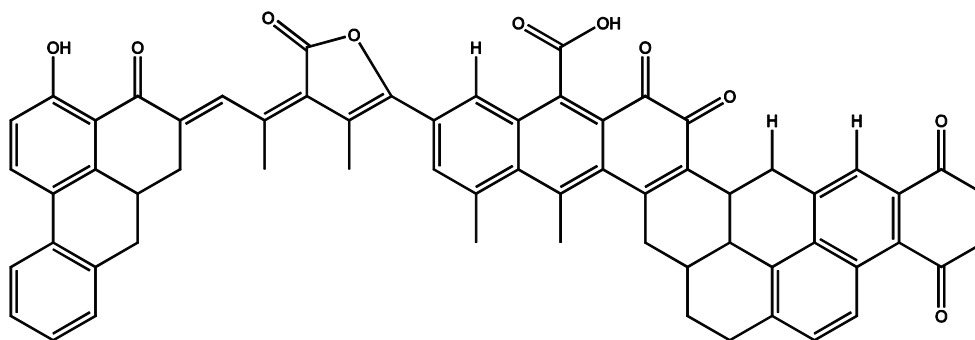
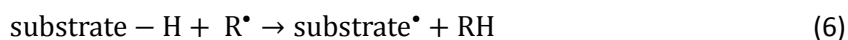


Fig. 15. Functional groups on a graphite surface [66].

Glassy carbon electrodes bear functional groups – COOH, phenolic OH and carboxyl groups – or hydrogen on the surface [66]. Fig. 15 shows some examples for possible functional groups on a carbon surface. For the electrolyte studies this is an important fact. Silicon surfaces have been electrochemically grafted by Grignard reagents. The process is described by reactions (5)-(7) [67]:



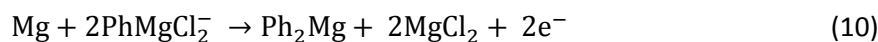
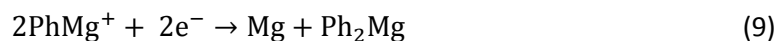
The emerging radical attacks the hydrogen atoms on the surface and another Grignard molecule modifies the substrate. If R equals an aryl-group even multilayers of this group can cover the surface [67]. So in the case of the investigated electrolytes (all contain PhMgCl) the GC surface might be electrografted during cycling which leads to a phenyl group covered surface with totally different electrochemical properties compared to a freshly polished one. This results in lower current efficiencies due to a lot of side reactions.

For further characterization of the particular electrolytes NMR-studies were used to identify the anionic species. The identification of the equilibrium species in solution is of great importance to understand the electrode reaction mechanisms of the Mg deposition and dissolution.

5.2.1 1 M PhMgCl in THF

The cyclic voltammograms in Fig. 16 indicate a nearly reversible Mg deposition/dissolution with current efficiencies up to 98.6 %. This is possible due to following

reactions (8)–(10) with PhMg^+ as active ion species and PhMgCl_2^- as stabilizing anion [29]:



These reactions are based on the Schlenk equilibrium (equation (11)) of Grignard solutions:

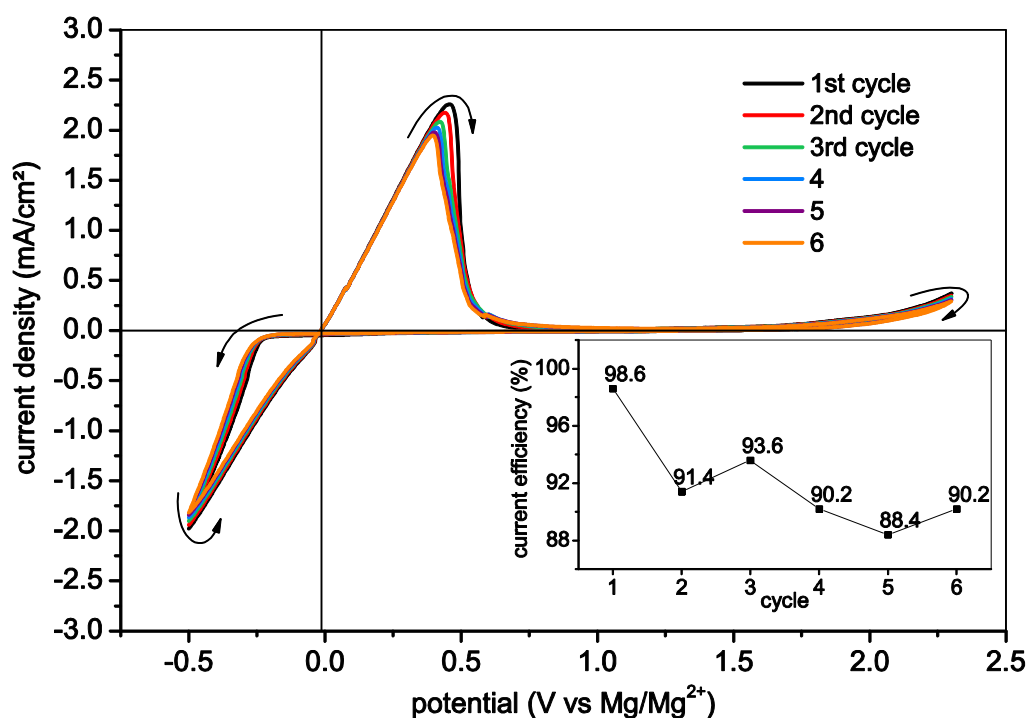
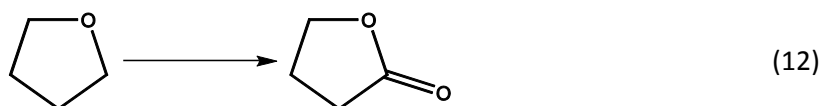


Fig. 16. Cyclic voltammograms of continuously repeated 6 cycles of 1 M PhMgCl in THF on Pt electrode, $\nu = 50 \text{ mV/s}$ at 30°C ; start from the OCP = 1.1 V in positive direction.

The **anodic stability** of the Grignard electrolyte depends according to Guo *et al.* on the nature of the Mg-R bonding. The more electron withdrawing a substituent is, the higher the oxidative stability of the Grignard solution [29]. The decomposition of this electrolyte starts at approx. 2.1 V. This would fit into the predicted order: FPhMgBr (2.4 V) > PhMgBr (1.8 V) > EtMgBr (1.5 V). Chloride (being more electronegative than bromide) seems to stabilize the aryl Grignard compound. At the anodic limit the THF is oxidized to γ -butyrolactone [68]:



Variation of the scan rate in cyclic voltammetry of the pure Grignard solution (Fig. 17 top) showed a decrease of the anodic peak potential and anodic peak current with increasing scan rate. The $\Delta E_p^{ox}/\Delta i_p^{ox}$ values (Table 9) show that this observed effect is due to a high iR drop of the THF based Grignard solution.

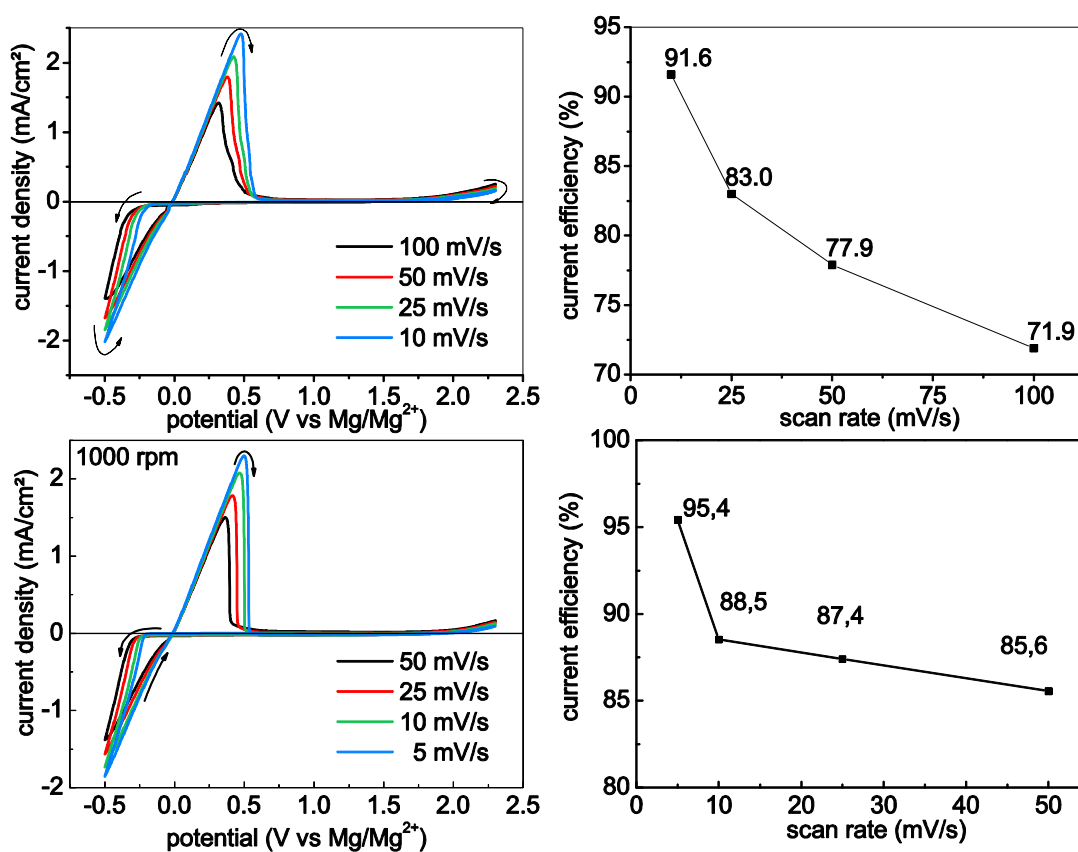


Fig. 17. Cyclic voltammograms of 1 M PhMgCl at Pt disk electrode with scan rates between 10-100 mV/s (top) and RDE voltammograms with scan rates between 5-50 mV/s (bottom); start from the OCP in positive direction

Table 9: Anodic peak potential and peak current Δ values for the CV scan rate experiments of 1 M PhMgCl on Pt at $T = 30^\circ\text{C}$

Measurement used for Δ calculation	ΔE_p^{ox} (mV)	Δi_p^{ox} (mA)	$\Delta E_p^{ox}/\Delta i_p^{ox}$ (Ω)
CV _{10 mV/s} – CV _{25 mV/s}	54.43	0.02331	2335
CV _{25 mV/s} – CV _{50 mV/s}	44.88	0.02063	2175
CV _{50 mV/s} – CV _{100 mV/s}	60.07	0.02642	2273

The same observation was made by performing rotating disk electrode experiments (see Fig. 17 bottom and Table 10). If changing the scan rate from 5 mVs⁻¹ to 50 mVs⁻¹ at a constant rotation rate of 1000 rpm, this results in a decrease of the peak potential and current while applying a faster scan rate.

Table 10 Anodic peak potential and peak current Δ values for the RDE scan rate experiments of 1 M PhMgCl on Pt at $T = 30^\circ\text{C}$

Measurement used for Δ calculation	ΔE_p^{ox} (mV)	Δi_p^{ox} (mA)	$\Delta E_p^{\text{ox}}/\Delta i_p^{\text{ox}}$ (Ω)
CV _{5 mV/s} – CV _{10 mV/s}	37.59	0.01561	2408
CV _{10 mV/s} – CV _{25 mV/s}	50.59	0.02100	2409
CV _{25 mV/s} – CV _{50 mV/s}	50.84	0.02002	2539

In additional cyclic voltammetry scans at $v = 50 \text{ mV s}^{-1}$ the **cathodic limit** was varied from -0.5 V to -0.8 V (Fig. 18). The current efficiency increased the more negative the cathodic limit became. Here again the time scale is important. A more negative cathodic potential favors more nucleation and enables more Mg to deposit on the electrode.

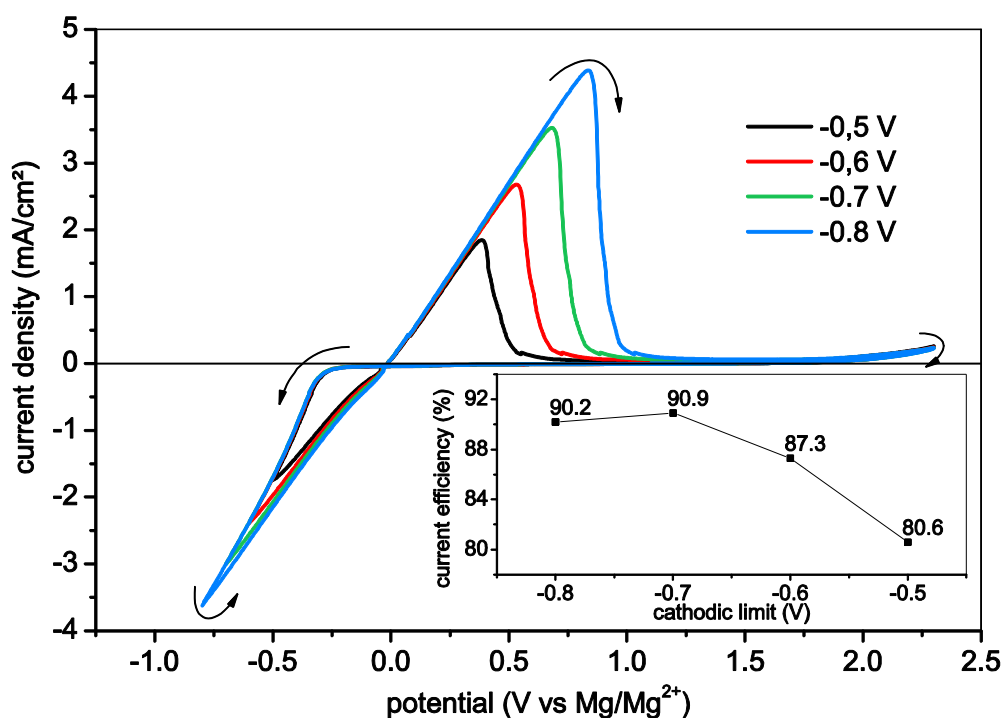


Fig. 18. CV for Mg deposition/dissolution from 1 M PhMgCl electrolyte on Pt electrodes at $v = 50 \text{ mV/s}$ and 30°C . The cathodic limit varies from -0.5 V to -0.8 V; start from the OCP = 1.1 V in positive direction.

To investigate how different rotation rates affect magnesium deposition, **RDE measurements** were carried out at $v = 50 \text{ mVs}^{-1}$ and the rotation rates were varied from 100-1500 rpm. Even for higher rotation rates no limiting cathodic current was obtained, which would have been indicated by a current plateau.

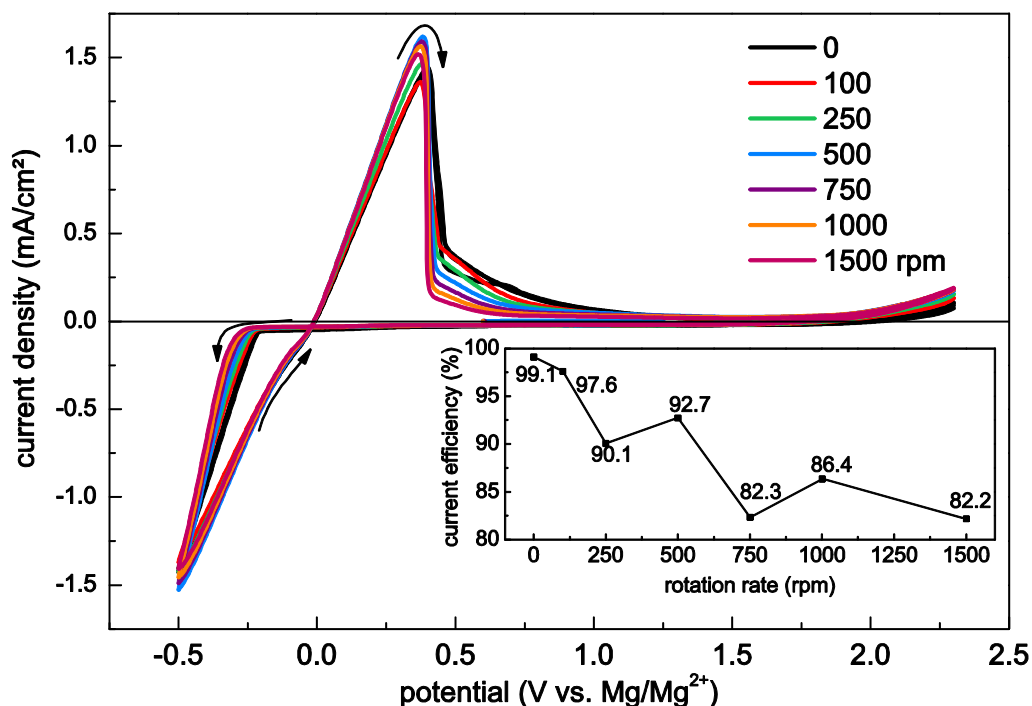


Fig. 19 Rotation disk voltammograms at $v = 50 \text{ mVs}^{-1}$ of 1 M PhMgCl on Pt at 30°C. The rotation rates vary from 0-1500 rpm: start from the OCP in positive direction.

However, in this experiment a drop of the current efficiency with increasing rotation rate can be observed. This effect implies that less Mg is deposited and the additional cathodic charge is due to decomposition of the electrolyte. Due to the Schlenk equilibrium (equation 11) there are different magnesium compounds in solution. If the formation of an intermediate is involved in the deposition process, the hydrodynamic force obviously drives away this intermediate Mg species from the electrode into the bulk.

5.2.1.1 Diffusion coefficient

Two different methods were used to determine the diffusion coefficient of the electrochemical active ion species in solution:

The data of chronoamperometry experiments was used to calculate the diffusion coefficient of the electroactive ion species using the Cottrell equation, which describes the diffusion controlled current with time [60]:

$$I = \frac{nFA C_0 \sqrt{D}}{\sqrt{\pi}} \cdot \frac{1}{\sqrt{t}} \quad (13)$$

t ...time [s],
 C_0 ...concentration [mol/cm³],
 A ...electrode area [cm²],
 I ...current [A]

D ...diffusion coefficient [cm²/s],
 F ...Faraday constant [C/mol],
 n ...number of electrons

Another method – chronocoulometry – is used to detect the cumulative charge vs. time. The Anson equation links the charge with the square root of time.

$$Q = \frac{2nFA C_0 \sqrt{D}}{\sqrt{\pi}} \cdot \sqrt{t} \quad (14)$$

t...time [s]

*C*₀...concentration [mol/cm³]

A...electrode area [cm²]

Q...charge [C]

D...diffusion coefficient [cm²/s]

F...Faraday constant [C/mol]

n...number of electrons

Rotating disc electrode measurements are based on controlled mass transport by rotating the working electrode. With this method it is possible to estimate the reaction rate, to explain reaction mechanisms and to find intermediates. The convective flux as a result of the rotating electrode causes a steady concentration gradient at the electrode. So if the solution is non-vortical the rotation rate and the diffusion limiting current can be described by the Levich equation [60]. However, in the experiments no limiting current was observed, therefore the Levich equation could not be used.

Fig. 20 depicts the chronoamperogram and the chronocoulogram for different potentials to initiate Mg deposition. A more negative potential step resulted in a higher current but unfortunately, no limiting current value was obtained.

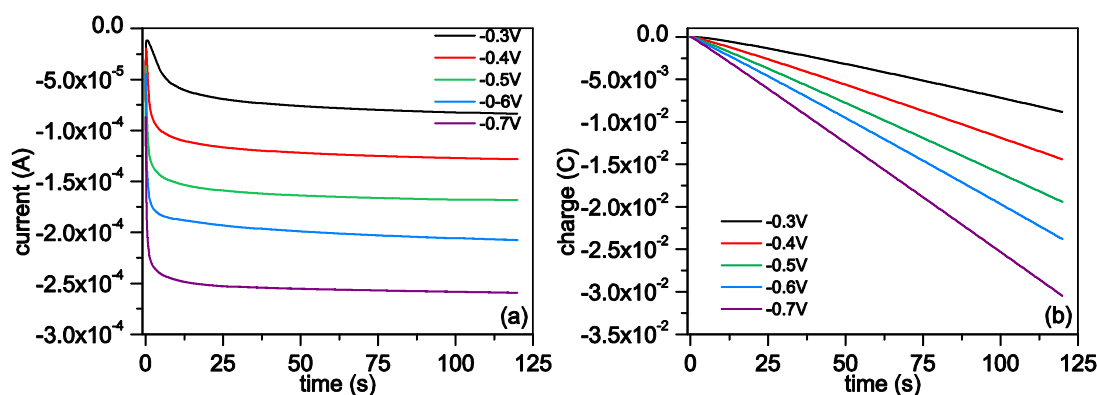


Fig. 20 Chronoamperogram (a) and chronocoulogram (b) of 1 M PhMgCl at different potentials.

The calculation of the diffusion coefficient in this electrolyte by means of the measured current was not possible since the decomposition of the electrolyte interfered with the deposition of magnesium.

5.2.2 0.25 M APC in THF

As mentioned in literature the current efficiency of each cycle can vary up to 40 % depending on the cycle number [68]. In general, early cycles show less current efficiency for most electrolytes and reach a limiting value after a certain number of cycles. The

cyclization experiment in APC electrolyte reflects this common observation (Fig. 21). The current efficiency increases with each cycle and approaches a limit at 96.5 %.

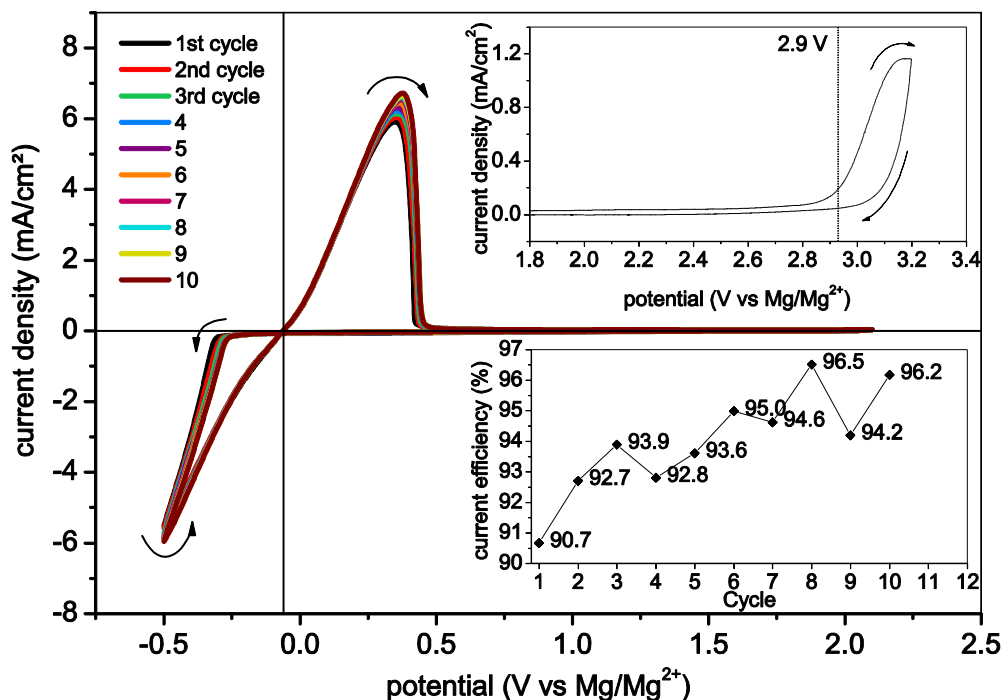
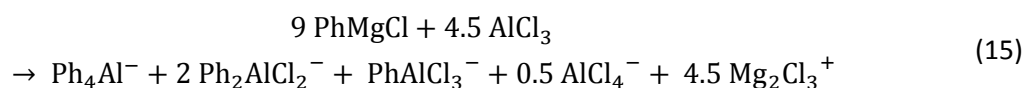


Fig. 21. CV of continuously repeated 10 cycles of 0.25 M APC in THF on Pt electrode, $\nu = 50$ mV/s at 30°C (OCP = 2.05 V)

This electrolyte shows a high **anodic stability** of about 2.9 V, together with a low onset deposition potential (-240 mV) and the stripping peak potential seems to be independent of the **scan rate** (Fig. 22). The ion species in this electrolyte have been identified with Raman spectroscopy, multinuclear NMR and single crystal XRD analysis by Pour *et al.* [63]. Mg_2Cl_3^+ is assumed to be the main cation and active ion species. MgCl^+ , which was primarily also supposed to allow reversible Mg deposition/dissolution, could only be detected by SCXRD and therefore it is unclear if it really exists in solution. The highly complex equilibrium of this electrolyte is shown in the following equation (15):



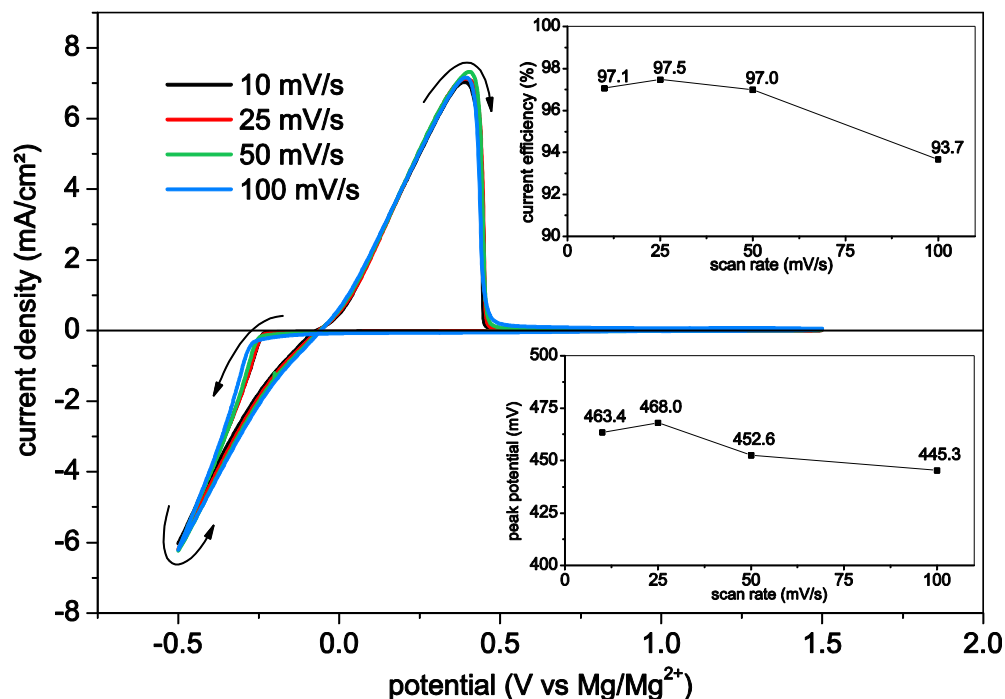


Fig. 22 Cyclic voltammograms of 0.25 M APC on Pt at 30°C. The scan rates vary from 10-100 mV s⁻¹.

Furthermore, the variation of the cathodic limit did not seem to affect the coulombic efficiency in any way. If the **cathodic limit** is changed from -0.5 V to -1.0 V the current efficiency only varies by 5 % (Fig. 23). In this experiment a cathodic peak can be observed if scanning a wider cathodic area, so the determination of a diffusion coefficient by chronoamperometry experiments can be considered feasible.

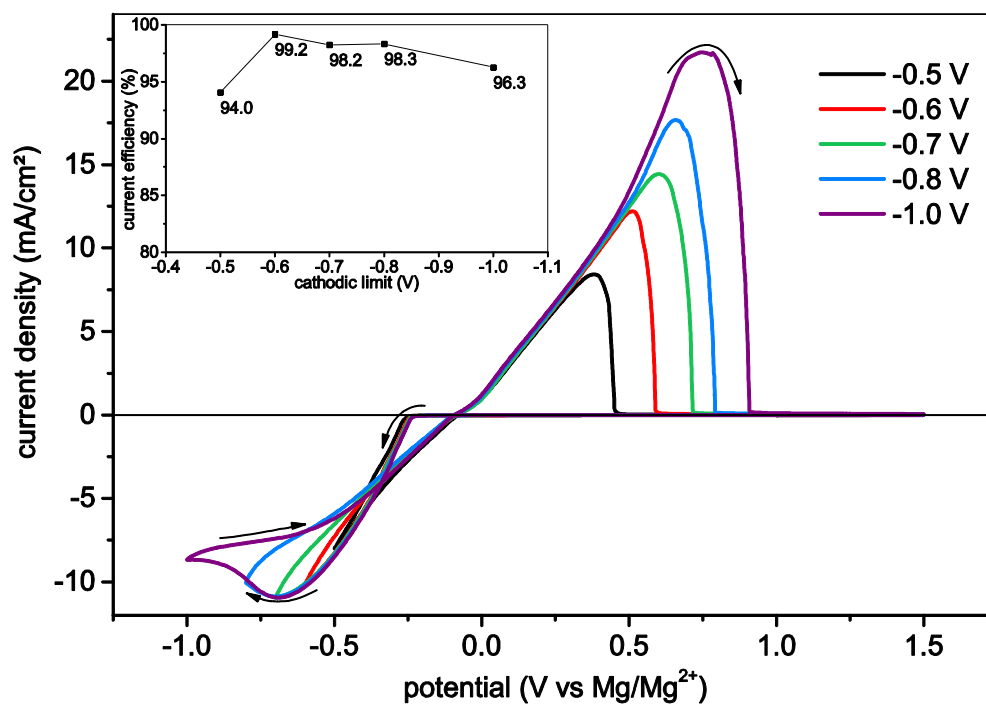
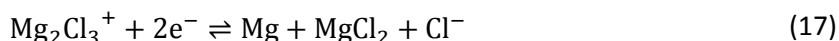


Fig. 23 CV for Mg deposition/dissolution of 0.25 M APC on Pt electrodes at $v = 50$ mV/s and 30°C. The cathodic limit varies from -0.5 V to -1.0 V.

5.2.2.1 Diffusion coefficient

Like for the 1 M PhMgCl electrolyte the diffusion coefficient in the 0.25 M APC solution was estimated by chronoamperometry and -coulometry experiments. The mechanism of magnesium deposition and stripping can involve either an electron transfer of two or four electrons because herein Mg ions are present as Mg_2Cl_3^+ in solution. Equation (16) - (18) show the possible mechanisms:



The work of Benmayza *et al.* [69] showed that the mechanism in a similar electrolyte (1:2 $(\text{C}_2\text{H}_5\text{MgCl})-(\text{C}_2\text{H}_5)_2\text{AlCl}_2/\text{THF}$) is based on a two electron transfer. Therefore all calculations have been done with $n = 2$.

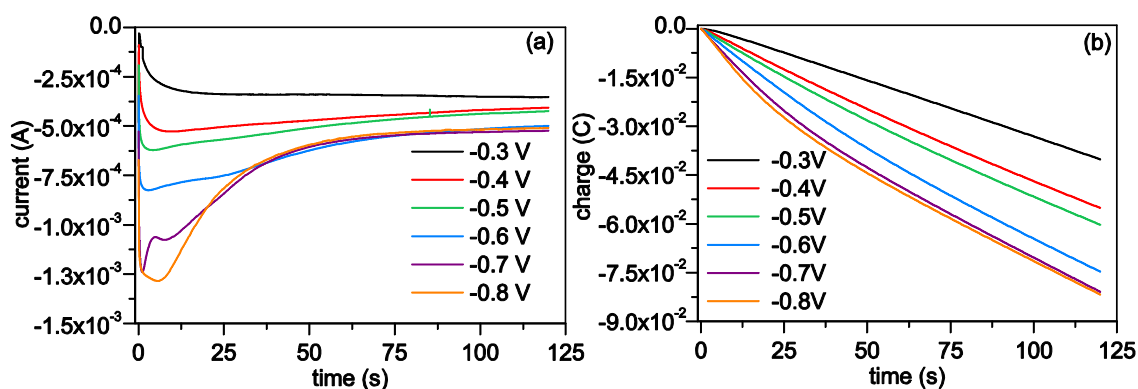


Fig. 24 Chronoamperogram (a) and chronocoulogram (b) of 0.25 M APC at different potentials.

The chronoamperogram in Fig. 24 (a) is approaching a limiting current value of $5.3 \cdot 10^{-4}$ A in the last 70 s of the experiment for the potentials -0.6 V to -0.8 V.

The diffusion coefficients determined by chronocoulometry and chronoamperometry show the same dependency on the applied potential (Fig. 25 and Fig. 26). The value rises with more negative potentials and is reaching a limit and becomes independent of the applied potential. The diffusion coefficient calculated by the Anson equation reaches a limit at about $6 \cdot 10^{-6} \text{ cm}^2\text{s}^{-1}$. The value calculated by Cottrell equals about $2 \cdot 10^{-6} \text{ cm}^2\text{s}^{-1}$. This little bit higher value gained in the Anson equation might be a result of integration.

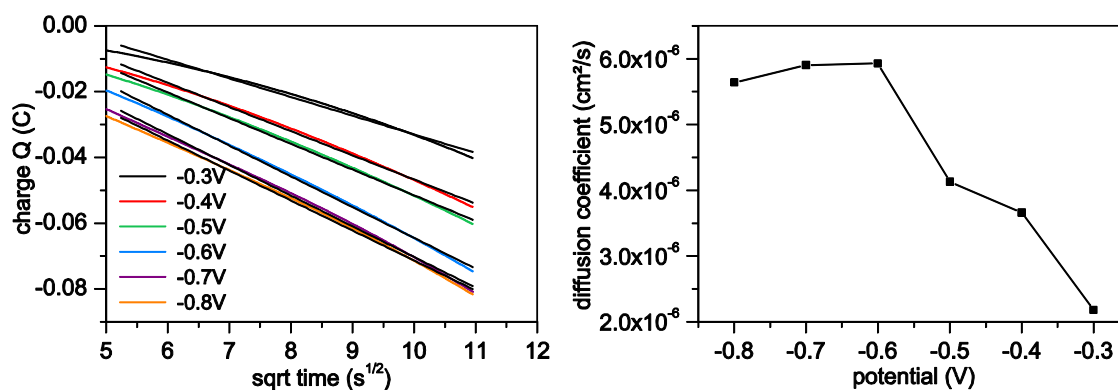


Fig. 25. Anson plot for different Mg deposition potentials (left). Diffusion coefficient dependency on the applied potential (right).

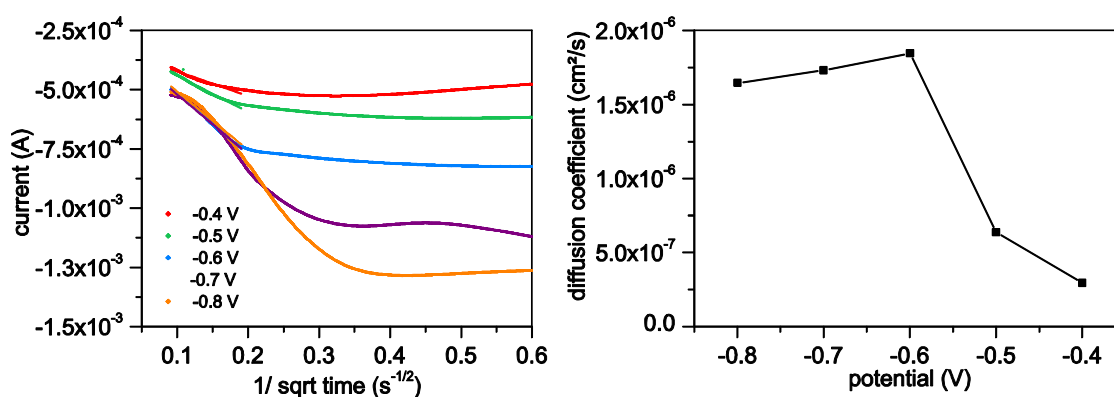


Fig. 26. Cottrell plot for different Mg deposition potentials (left). Diffusion coefficient dependency on the applied potential (right).

The apparent diffusion coefficient (between $D = 2 \cdot 10^{-6} \text{ cm}^2\text{s}^{-1}$ to $6 \cdot 10^{-6} \text{ cm}^2\text{s}^{-1}$) is one order of magnitude higher than for a similar 0.25 M 1:2 $(\text{C}_2\text{H}_5\text{MgCl})\text{-}((\text{C}_2\text{H}_5)_2\text{AlCl}_2)_2/\text{THF}$ electrolyte ($D = 1 \cdot 10^{-7} \text{ cm}^2\text{s}^{-1}$) [69]. Since both electrolytes are THF based and have the same concentration their viscosities might be quite similar and so their different ionic mobilities result in the higher ionic conductivity in 0.25 M APC solution. It equals about $\sigma = 3 \text{ mScm}^{-1}$ [31] compared to $\sigma = 0.1 \text{ mScm}^{-1}$ for the electrolyte mentioned first.

Furthermore, it must be mentioned that migration might have an impact on the determined diffusion coefficient. A lot of ionic species are present in solution, but no conducting salt could be used to prevent the effect of migration.

5.2.3 0.2 M BCF-PhMgCl in THF

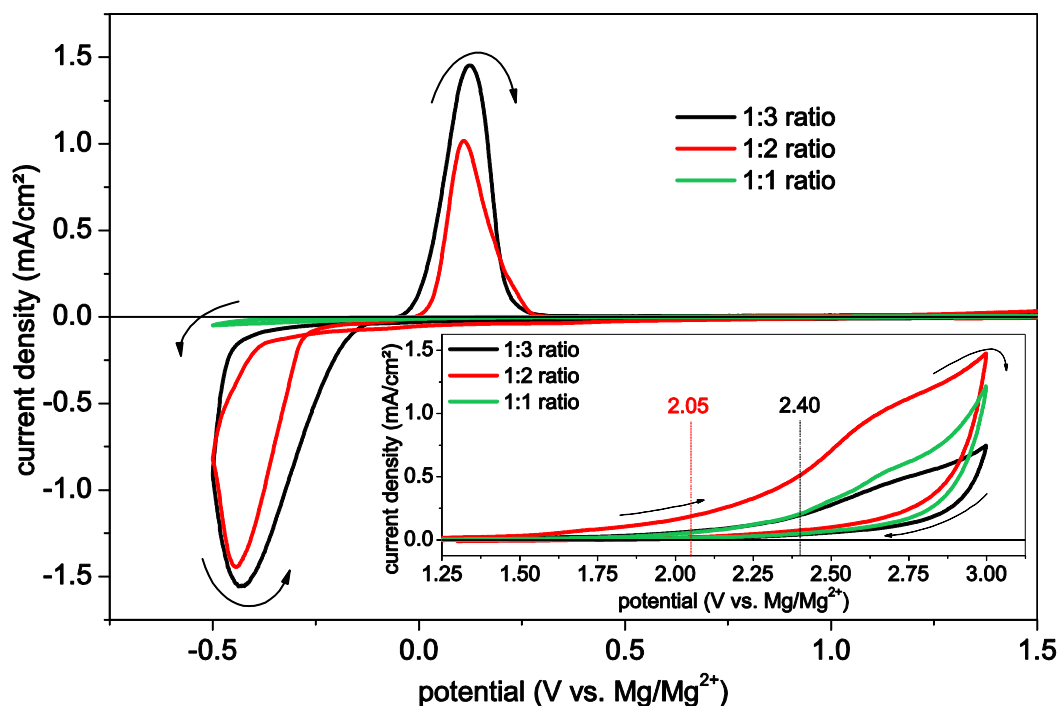


Fig. 27 Cyclic voltammograms of three different BCF-PhMgCl ratios on Pt at $v = 50 \text{ mV s}^{-1}$ at $T = 30^\circ\text{C}$. Inset shows the enlargement of the oxidation region to highlight the anodic stability of different ratios of the boron based electrolyte.

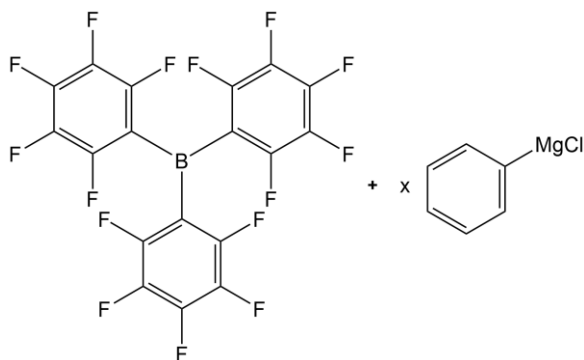


Fig. 28 BCF-PhMgCl electrolyte: different ratios of tris(pentafluorophenyl) borane and Grignard compound.

This boron based electrolyte was investigated due to its anodic stability of 3.7 V predicted by Muldoon *et al.* No further information on its electrochemical properties were presented [32]. This high anodic stability is assumed to be governed by the structure of the formed anion. The fluoro-substituted phenyl groups in $\text{B}(\text{C}_6\text{F}_5)_3(\text{C}_6\text{H}_5)^-$ have a strong electron withdrawing effect and should therefore shift the anodic stability to higher potentials.

Three different ratios of a 0.2 M solution were prepared (see 4.3.4) and their **anodic stabilities** range from 2.05 V to 2.40 V (Fig. 27). The best results according to the current efficiency, oxidative stability and current density is obtained with 0.2 M $\text{B}(\text{C}_6\text{F}_5)_3$ and 0.6 M PhMgCl ratio in THF. The high current density is due to the highest concentration of the active ion species. The 1:1 ratio did not show any deposition/dissolution peaks for Mg at all. The properties of the 1:2 and 1:3 electrolyte are summarized in Table 11:

Table 11: Properties of 1:2 and 1:3 BCF-PhMgCl electrolyte.

Property	1:3 ratio	1:2 ratio
Anodic limit	2.40 V	2.05 V
Highest current efficiency	86 %	62 %
Deposition onset potential	-300 mV	-450 mV
Viscosity	1.29 mPas ⁻¹	0.99 mPas ⁻¹

Since the 1:1 ratio is not reversible at all, further investigations were only done with the 1:3 and 1:2 ratio. The **variation of the scan rate** (Fig. 29) showed the following results:

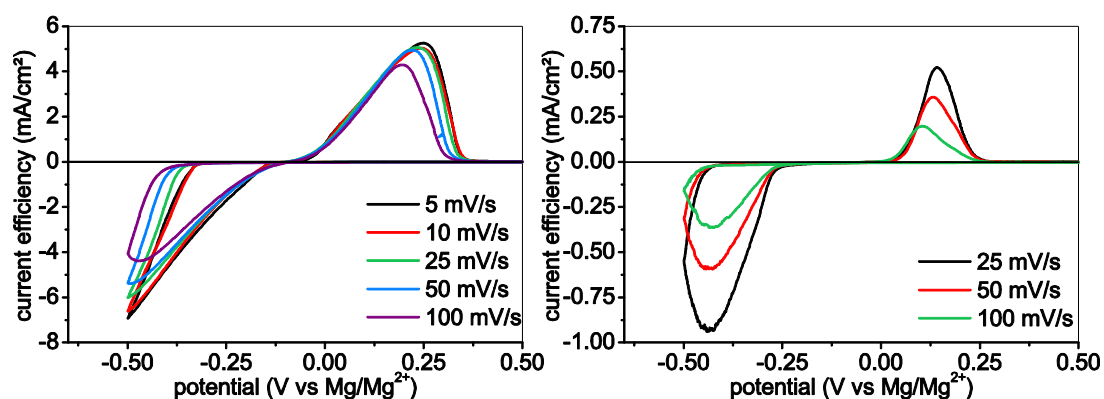


Fig. 29 Cyclic voltammograms of 0.2 M BCF-PhMgCl 1:3 (left) and 1:2 (right) electrolyte on Pt at 30°C. The scan rates vary from 5-100 mV s⁻¹ for the 1:3 ratio and from 25-100 mV s⁻¹ for the 1:2 ratio.

Qualitatively an impact of the scan rate can be observed. A higher scan rate leads to a decrease of E_p^{ox} and i_p^{ox} . It is more significant for the 1:2 than for the 1:3 ratio. But unlike the 1 M of PhMgCl in THF solution this effect is not due to an iR drop of the solution ($\Delta E_p^{ox}/\Delta i_p^{ox}$ values vary), its rather an effect of a slow electron transfer.

Further investigation of the boron-based electrolytes has been done by changing the **cathodic limit** from -0.5 V to -1.0 V for the 1:3 BCF-PhMgCl solution and from -0.4 V to -1.0 V for the 1:2 BCF-PhMgCl solution (Fig. 30). More negative potentials favor magnesium deposition, but for the 1:3 electrolyte the deposition rate of magnesium is apparently larger, indicated by the higher current density. In addition these CVs reveal the higher overvoltage for the onset deposition potential for 1:2 BCF-PhMgCl very clearly. It is about -150 mV higher for the 1:2 solution than for the 1:3 solution. This, of course, is another reason for less deposited Mg for the 1:2 electrolyte.

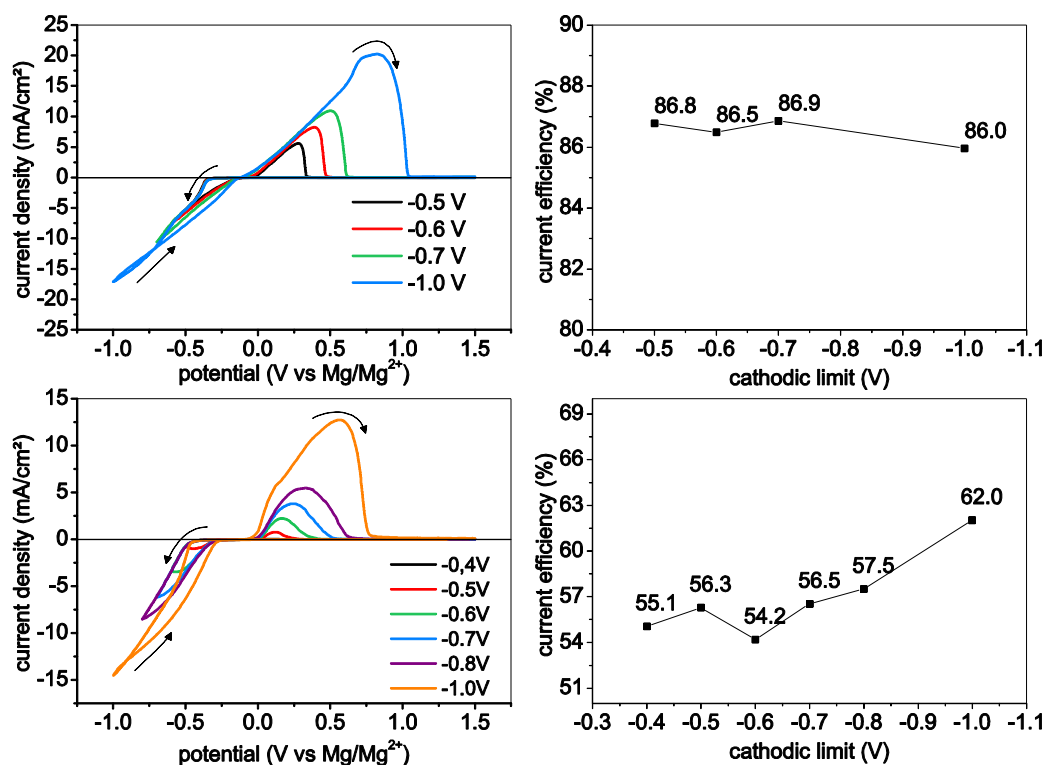


Fig. 30 CV for Mg deposition/dissolution from 0.2 M BCF:PhMgCl 1:3 (top) and 1:2 (bottom) on Pt electrodes at $v = 10$ mV/s and 30°C. The cathodic limit varies from -0.4 V to -1.0 V. The figures on the right display the corresponding CE of each measurement.

5.2.3.1 NMR studies

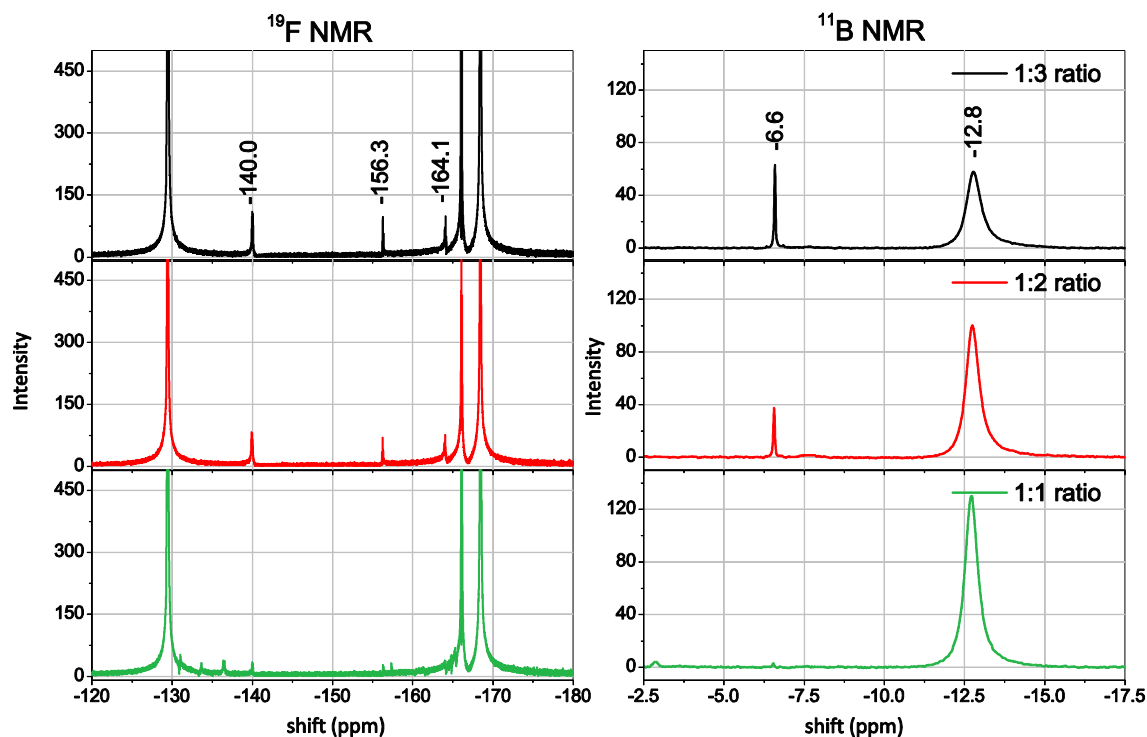


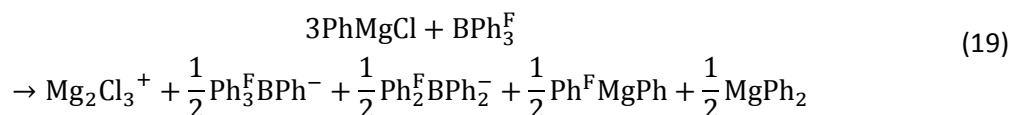
Fig. 31 The spectra on the left display the ^{19}F NMR of different ratios of BCF-PhMgCl, the spectra on the right show the ^{11}B NMR results.

For better understanding of the electrochemical properties of this electrolyte and for explaining the discrepancy of the predicted and measured anodic stability, NMR spectra were taken of the different ratios.

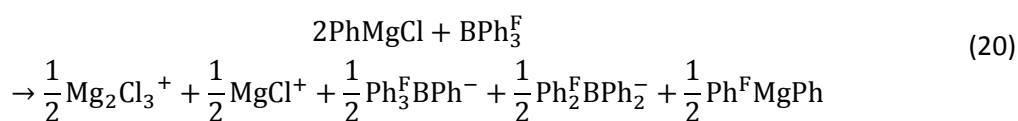
The ^{11}B -NMR spectra display two resonance lines for the 1:3 and 1:2 ratio and one for the 1:1 ratio; ^{11}B NMR (25 °C, D_2O , 96.3 MHz): $\delta = -12.8, -6.6$ ppm. Both resonances indicate the formation of borate anions. The same electrolytes have been characterized with ^{19}F NMR which confirms the existence of two different species $^{19}\text{F}\{^1\text{H}\}$ NMR (25 °C, D_2O , 282.4 MHz): $\delta = -168.4$ (t, *m*-CF), -166.1 (t, *p*-CF), -129.5 (d, *o*-CF); $\delta = -164.1$ (m, *m*-CF), -156.3 (t, *p*-CF), -140 (m, *o*-CF). It also suggests that both tetra-coordinated boron species are fluorinated. Higher Grignard content favors evidently the formation of a second symmetrical (due to the sharp line at -6.6 ppm) boron species.

The following equations (19)-(21) propose the existing equilibrium species in the BCF electrolyte at different molar ratios.

1:3 ratio



1:2 ratio



1:1 ratio



In the 1:1 ratio there is formal no existence of the Mg_2Cl_3^+ cation which is responsible for the reversible Mg deposition/dissolution reaction [63], so this might explain why no Mg deposition was observed for this electrolyte.

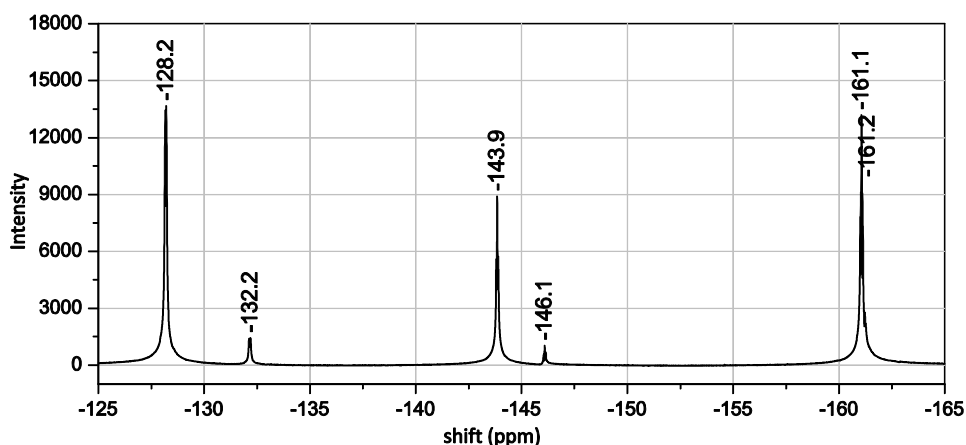


Fig. 32 ^{19}F NMR spectrum of tris(pentafluorophenyl)borane in CD_2Cl_2 .

The NMR analysis of the starting material for the electrolyte solution showed the characteristic resonance lines for tris(pentafluorophenyl)borane $^{13}\text{C}\{^1\text{H}\}$ NMR (25 °C, CD_2Cl_2 , 126 MHz): δ = 113.5 (br, *ipso-C*), 138.0 (dm, *m-CF*, $^1J(^{13}\text{C}-^{19}\text{F}) = 253$ Hz), 145.6 (dm, *p-CF*, $^1J(^{13}\text{C}-^{19}\text{F}) = 262$ Hz), 148.8 (dm, *o-CF*, $^1J(^{13}\text{C}-^{19}\text{F}) = 256$ Hz). $^{19}\text{F}\{^1\text{H}\}$ NMR (25 °C, CD_2Cl_2 , 470 MHz): δ = -161.1 (d, *m-CF*), -143.9 (m, *p-CF*), -128.2 (m, *o-CF*). [70]. However, an impurity of 9 % comes with it, indicated by three smaller resonances in the ^{19}F -NMR at δ = -132.2, -146.1, -161.2. These lines have the same coupling information and integral ratio like those for $\text{B}(\text{C}_6\text{F}_5)_3$. The shifts and J-coupling point to bis(pentafluorophenyl)boronic acid as impurity [71]. This might be a likely reason for the early decomposition of the electrolyte.

5.2.4 Saturated MACC in THF electrolyte

This electrolyte comprises two inorganic salts, MgCl_2 and AlCl_3 in THF. Fig. 33 depicts the cyclic voltammetry of the solution. The current efficiency is rather low with only 57 %, the **anodic stability** is 3.0 V, though (Fig. 34 a). Unfortunately, this electrolyte shows a high overpotential for the magnesium deposition of about -890 mV in the first cycle decreasing to -640 mV in the 10th cycle (Fig. 34 b). At the same time, the low solubility of MgCl_2 in THF limits the current density, here to 3.2 mA cm^{-2} .

An anomaly in MACC is the detection of background current, unlike the other electrolytes. In this solution obviously irreversible side reactions occur (bottom inset in Fig. 33). They are most likely due to Al deposition and oligomerization products of THF caused by AlCl_3 [72]. The background current due to these side reactions superimposes with the deposition of magnesium and impedes the calculation of the current efficiency.

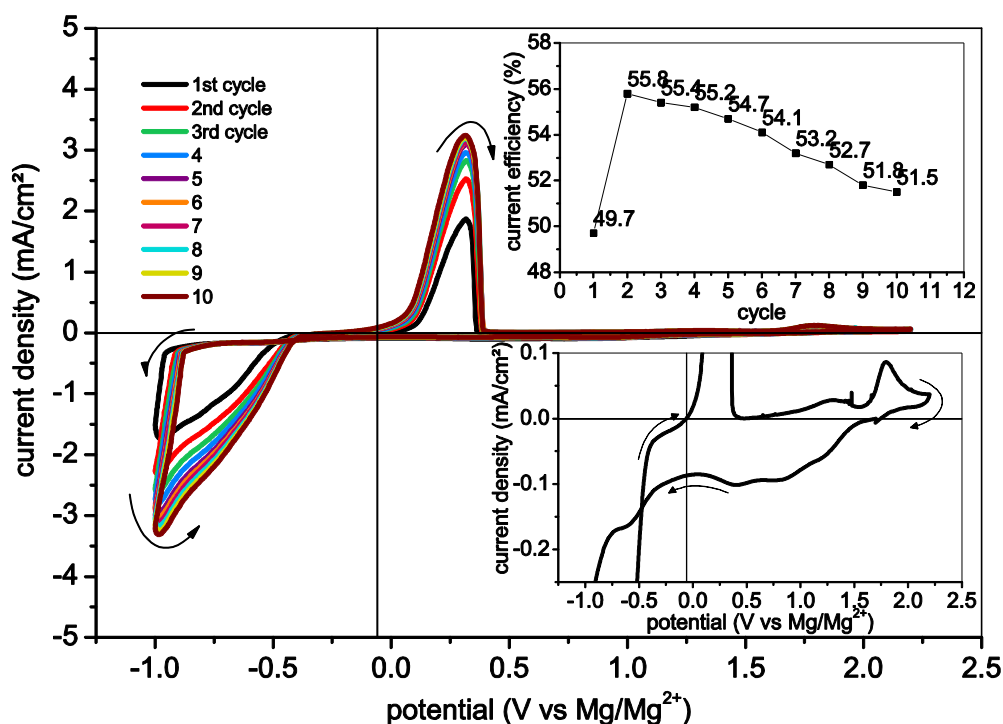


Fig. 33 Cyclic voltammogram of continuously repeated 10 scans of 1:2 MACC in THF on Pt electrode, $\nu = 50 \text{ mV/s}$ at 30°C (OCP = 1.7 V). The inset on top shows the current efficiency of each cycle while the one on the bottom displays current of the side reaction.

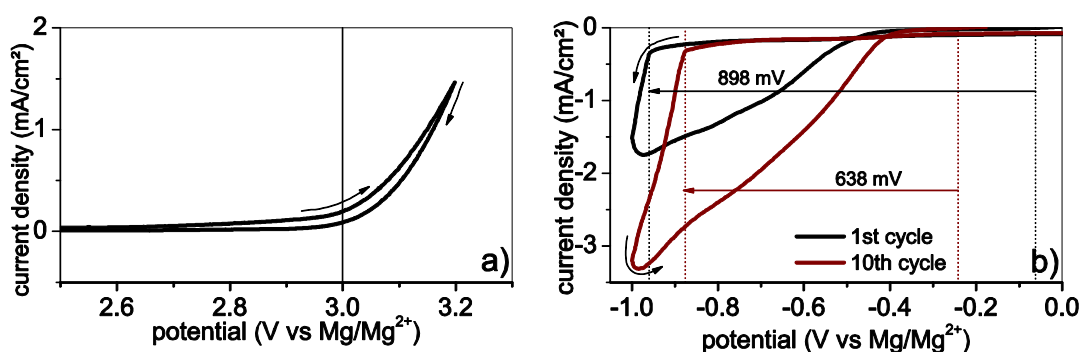


Fig. 34 Enlargement of the oxidation region to highlight the anodic stability of MACC, $\nu = 50 \text{ mV s}^{-1}$, Pt, 30°C (a) and enlargement of the cathodic limit to display the onset potential for the deposition of magnesium, $\nu = 50 \text{ mV s}^{-1}$, Pt, 30°C (b).

In contrast to the pure Grignard solution, the MACC electrolyte reveals a different dependency of the anodic peak potential on the **scan rate** (Fig. 35). If increasing the scan rate, the anodic peak potential increases likewise. This fact, together with the high onset potential for magnesium deposition suggests a slow electron transfer in this electrolyte.

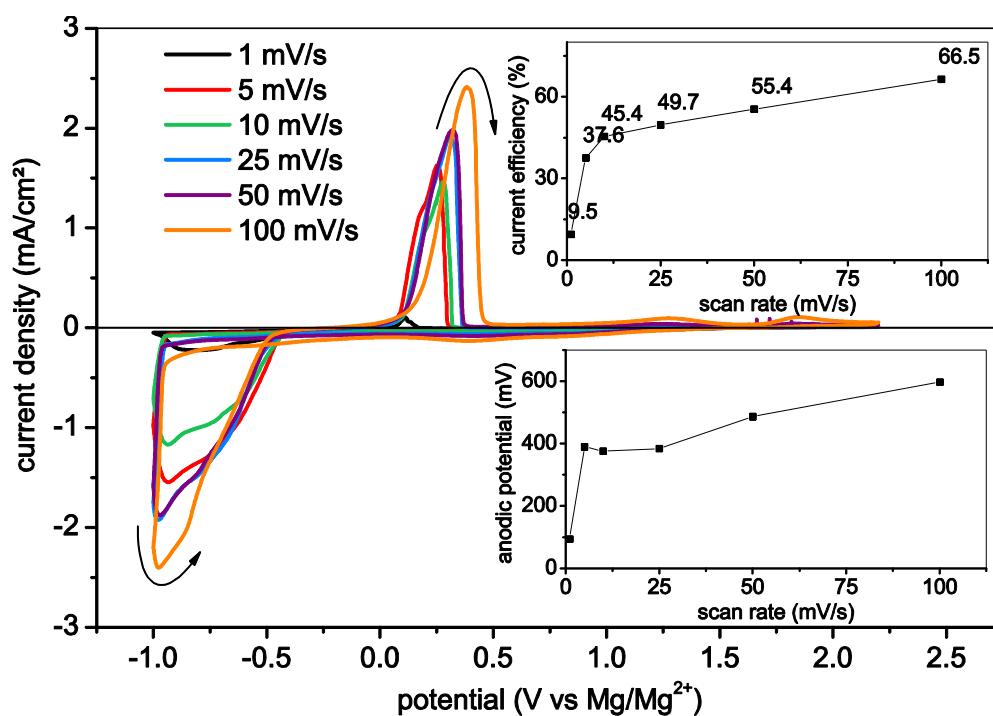


Fig. 35 Cyclic voltammograms of sat. MACC on Pt working electrode with scan rates between 1-100 mV/s.

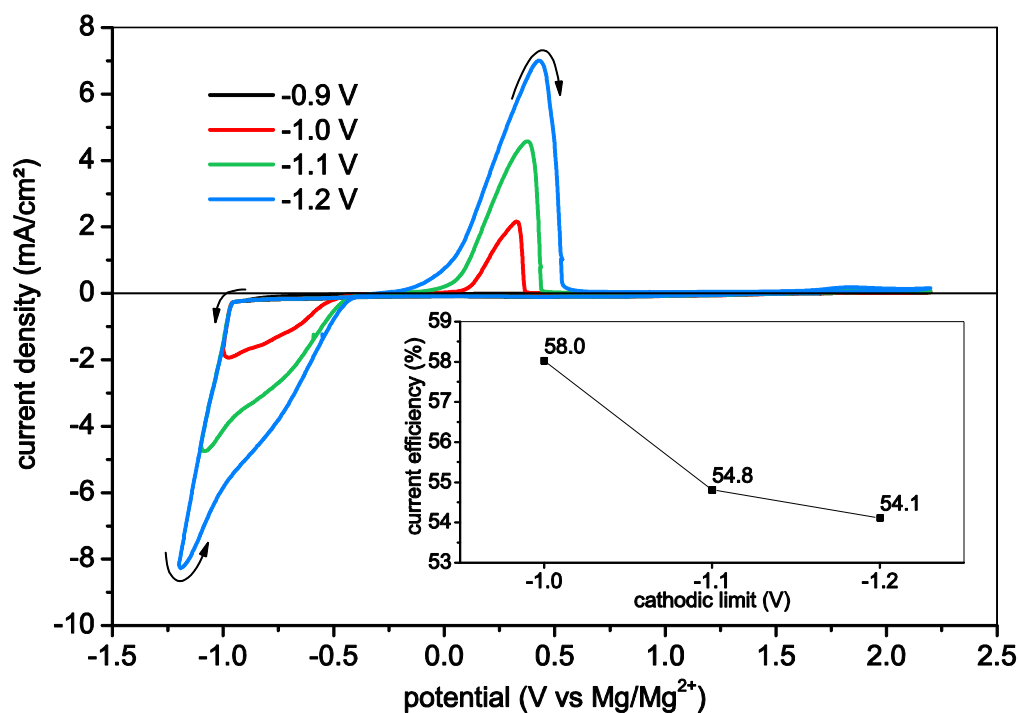


Fig. 36 Cyclic voltammograms for Mg deposition/dissolution of sat. MACC electrolyte on Pt electrodes at $v = 50$ mV/s and 30°C. The cathodic limit varies from -0.9 V to -1.2 V.

Interestingly, it also shows different properties if changing the **cathodic limit** (-0.9 V – -1.2 V) to more negative potentials compared to the 1 M phenylmagnesium chloride solution (Fig. 36). First of all, the scan to -0.9 V did not show any magnesium

deposition because of the very negative onset potential for magnesium deposition in this electrolyte. By going more and more negative, more magnesium can be plated on the working electrode. However, a more negative potential results in less current efficiency. This is due to the charge consumed by the side reaction. Because it interferes with the deposition of magnesium, it also affects the net current efficiency.

5.2.4.1 NMR studies

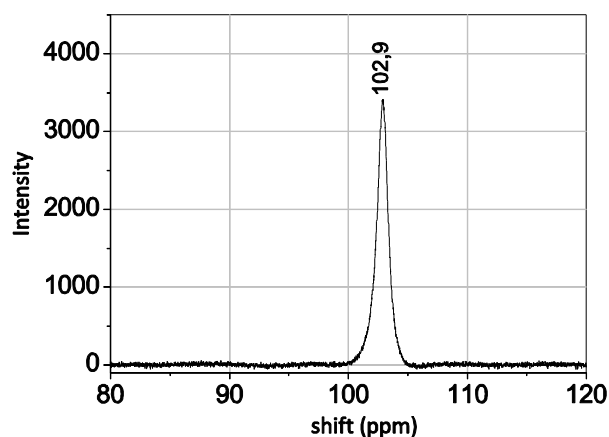


Fig. 37 ^{27}Al NMR spectrum of MACC at 78.2 MHz, 25°C, external lock signal D_2O .

Further investigation of this electrolyte has been done by ^{27}Al -NMR. The resulting NMR shows a broad resonance line at $\delta = 102.9$ ppm. This confirms the formation of the AlCl_4^- anion [34]. Therefore the predicted ion species in solution are (equation (22)):



In this electrolyte only non-nucleophilic species are present and the reaction just involves a simple transmetallation from MgCl_2 to AlCl_3 . As a result one equilibrium anion species exists in solution. Hence, the improvement of the oxidative stability relies on this one anion, namely AlCl_4^- [34].

5.3 Characterization of anode alloys

For the Mg-ion battery an appropriate anode material has to be found. The electrochemical behavior of two different low alloyed magnesium metals is compared to pure Mg 99.9 %. For the exact composition of the alloys see section 4.1.2. The characterization has been done with cyclic voltammetry experiments in 0.25 M APC electrolyte. The setup is described in 4.4.1.1 but instead of a magnesium foil platinum gauze served as counter electrode.

5.3.1 Mg 99.9 %

The pure magnesium is studied as reference to see how alloying elements affect the performance. The cycling capacity of the anode was tested by performing three repeating scans in CV experiments. The voltammetric cycling started at 0 V (OCP = +0.032 V) either in anodic (positive scan) or cathodic direction (negative scan). If scanning in positive direction Mg was first dissolved and then re-deposited. Negative scans required an active ion species in solution to be able to deposit Mg at all.

Fig. 38 shows the multicycles initiated in cathodic (a) or anodic (b) direction. A distinct characteristic can be observed. The first cycle in both directions shows an overpotential between 200-300 mV for magnesium deposition/dissolution. The second and third cycle are much more reversible. Probably the magnesium is covered with a thin passive layer that causes this overpotential in the first cycle.

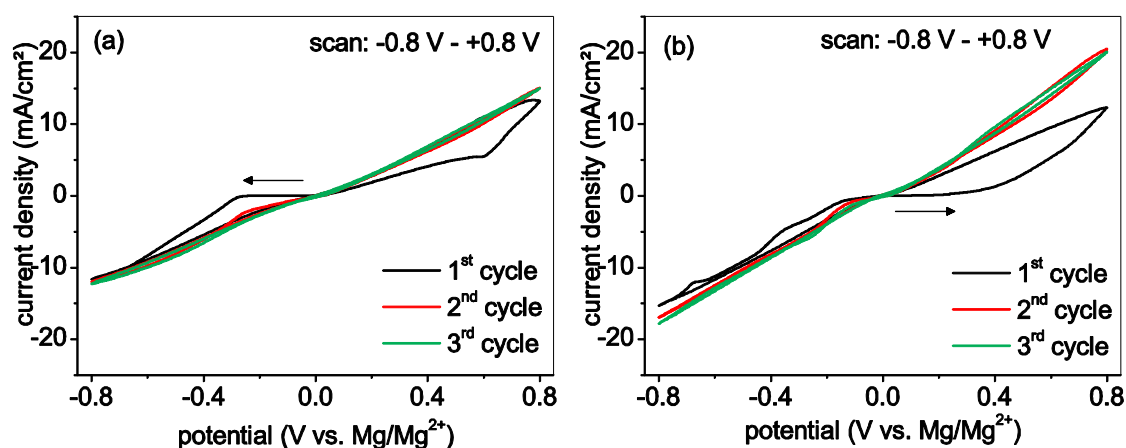


Fig. 38. Three voltammetric cycles of Mg 99.9 % starting in negative direction (a) and three voltammetric cycles starting in positive direction (b) in 0.25 M APC solution, $\nu = 10 \text{ mVs}^{-1}$ at 30°C .

Mg 99.9 % was cycled at different scan rates. Fig. 39 shows the scan rate experiments at 10, 50 and 100 mV and the corresponding charge vs. time graphs. In each first cycle an overpotential is observed that disappears for the second and third cycle. Here, slightly asymmetric potential cycles have been performed (-0.8 V - +1.0 V). This engenders more dissolved magnesium, so in the first cycle a short drop in current density at 0.8 V can be observed when all the previously plated magnesium has been dissolved and it increases

again when the alloy starts to dissolve. The shift in the base line in the charge vs. time plots is again due to the asymmetric scan.

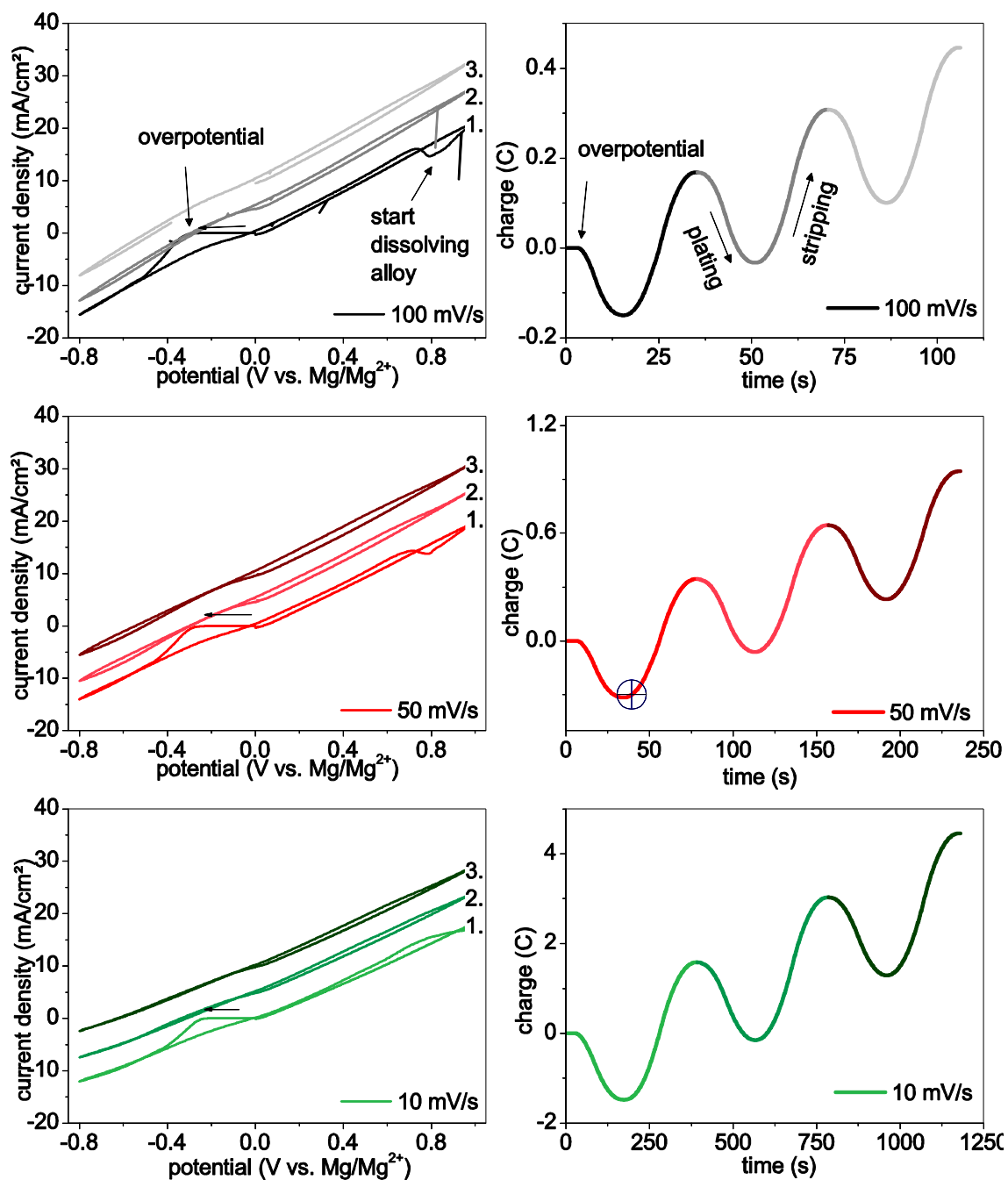


Fig. 39 Cyclization experiments of Mg 99.9 % in 0.25 M APC at 100, 50 and 10 mV/s⁻¹. For a better visualization of each cycle, cycle 2 and 3 have been shifted upward by a constant current density of 5 mA/cm².

During cycling the deposition of black particles was observed on the working electrode. These are assumed to be MgO particles which poorly adhere on the electrode surface and can be therefore found as precipitates in solution after a while. The precise content of oxygen in the alloy is unfortunately unknown. The effect of different oxygen

concentrations in the alloy will be measured in further experiments, but this is beyond this master thesis.

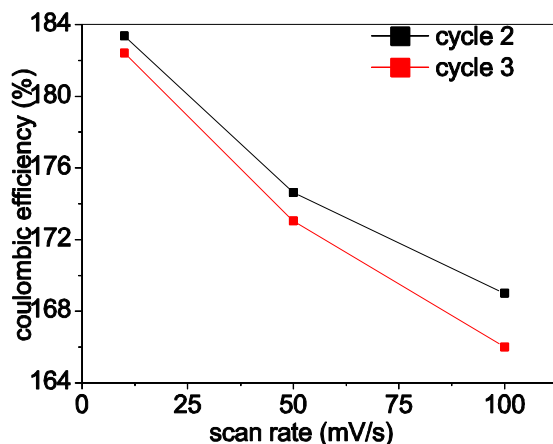
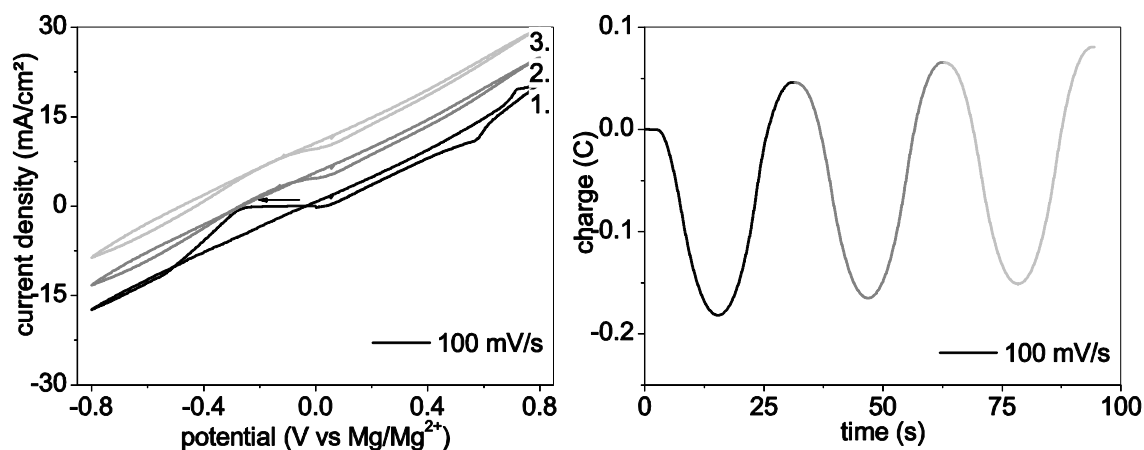


Fig. 40 Current efficiency of Mg 99.9 % for the last two cycles at different scan rates.

How the scan rate affects the current efficiency for electrodeposition can be taken from Fig. 40. It is higher than 100 % because of the asymmetric potential scan, but qualitatively a decrease in current efficiency with higher scan rate is noticed. This indicates that the side reaction (oxide formation) proceeds at a higher rate than the dissolution process. Less Mg is dissolved at higher scan rates. The current efficiencies only have been calculated for the last two cycles where no overpotential is observed.

5.3.2 MgGd

The alloy MgGd showed cycling behavior similar to Mg 99.9 %. Three cycles at 10, 50 and 100 mVs^{-1} were recorded and again an overvoltage for the first cycle was detected (Fig. 41). The voltammetric cycles have been performed symmetrically about the OCP (-0.8 V - 0 V - 0.8 V) starting in negative direction. Nevertheless, a minor shift in the baseline in the charge vs. time graphics occurred, due to more dissolved than deposited magnesium.



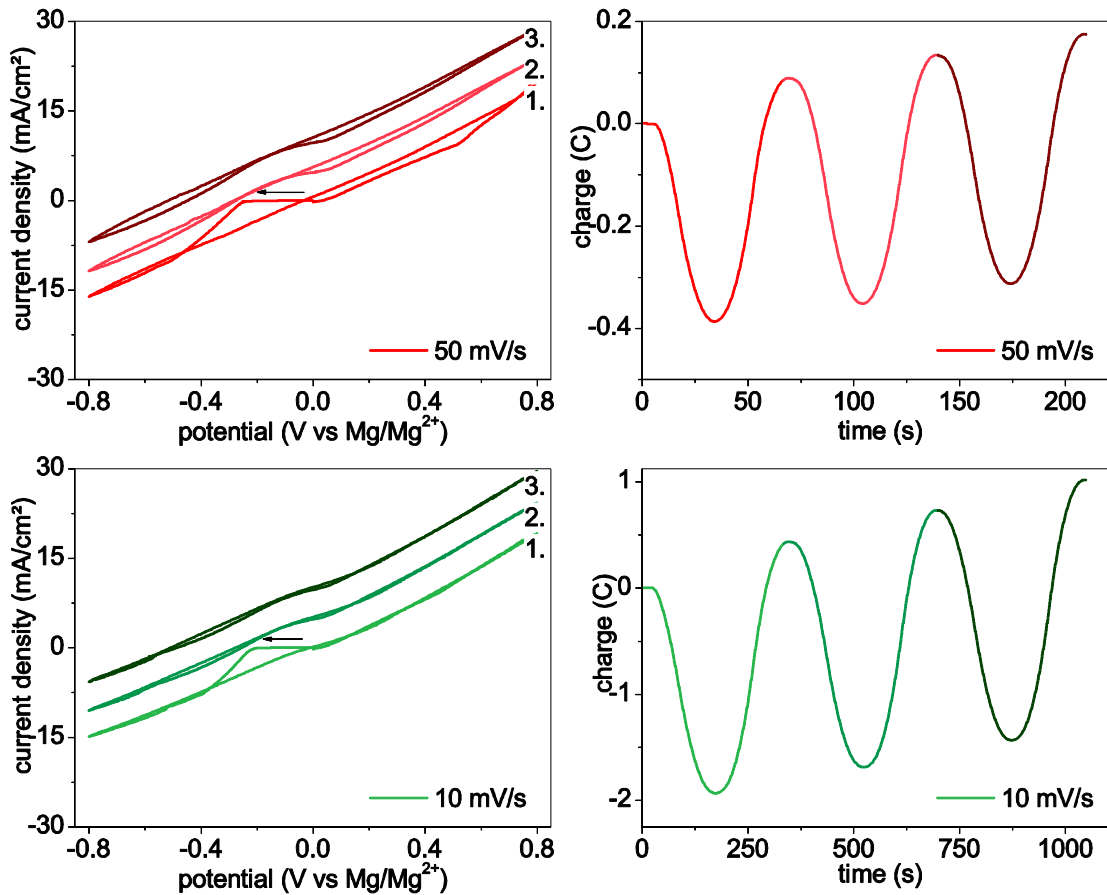


Fig. 41 Cyclization experiments of MgGd in 0.25 M APC at 100, 50 and 10 mVs^{-1} . For a better visualization of each cycle, cycle 2 and 3 have been shifted upward by a constant current density of 5 mA/cm^2 .

Equally to Mg without any alloying elements, black precipitates were found in the electrolyte. This corroborates the assumption that these particles are due to oxygen in the

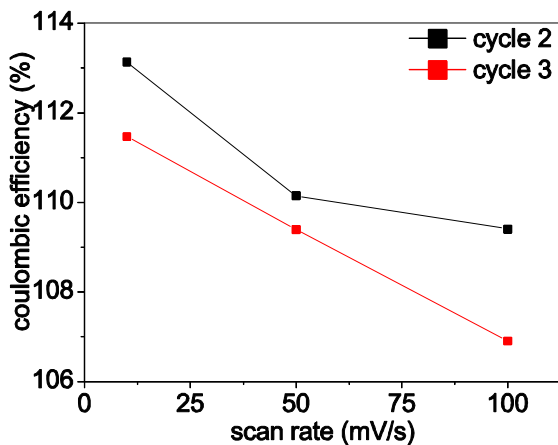


Fig. 42 Current efficiency of MgGd for the last 2 cycles at different scan rates.

alloy, which forms oxides with either magnesium or the alloying element. Since gadolinium has a standard potential (-2.28 V vs. NHE) similar to magnesium (-2.37 V vs. NHE) it might be dissolved and deposited as well. Gadolinium reveals no real effect on the cyclization behavior.

The dependency of the current efficiency for electrodeposition on the scan rate is analogous to pure Mg (Fig. 42). Higher scan rate yields lower current efficiencies. The formation of the oxide is faster than the dissolution process.

5.3.3 MgGdZn

The ternary alloy MgGdZn reveals the same cyclization characteristics like the previous anode materials. Fig. 43 displays the symmetrically performed (-0.8 V - 0 V - +0.8 V) cyclization experiments at $\nu = 10, 50$ and 100 mVs^{-1} . The overpotential of the first cycle is again 200-300 mV while the following cycles are more reversible.

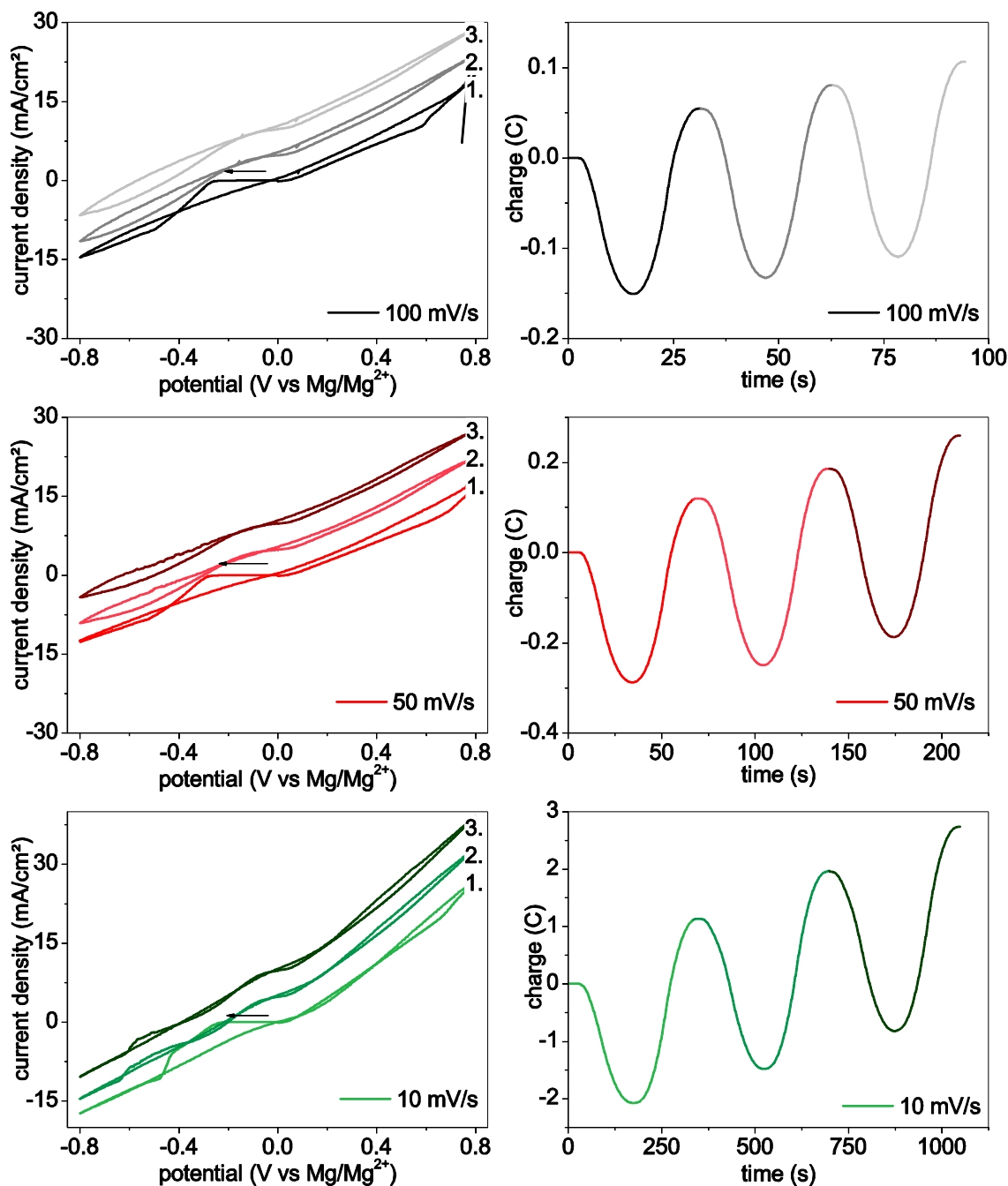


Fig. 43 Cyclization experiments of MgGdZn in 0.25 M APC at 100, 50 and 10 mVs^{-1} . For a better visualization of each cycle, cycle 2 and 3 have been shifted upward by a constant current density of 5 mA/cm^2 .

The cyclization experiment was leading to the formation of particles as well, but for this anode material these particles can be pure zinc or different oxides. Zinc is less negative (-0.76 V vs. NHE) than magnesium, so pure Zn precipitates in the alloy are not oxidized while the Mg matrix dissolves and so these particles can detach.

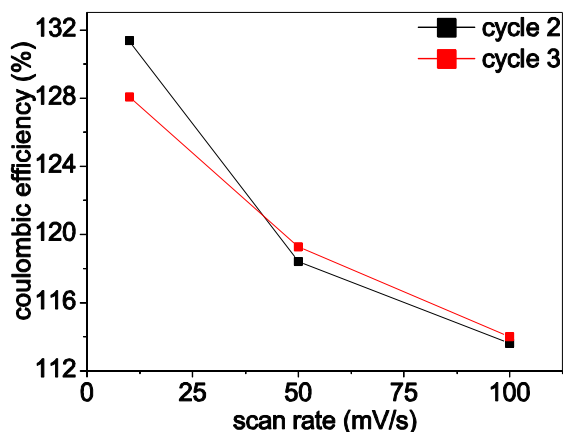


Fig. 44 Current yield of MgGdZn for the last 2 cycles at different scan rates.

For this alloy, the current efficiency for electrodeposition is again lower for higher scan rates (Fig. 44). This indicates that the deposition process has slow kinetics.

Like for gadolinium in MgGd, the additional element Zn does not seem to influence the cyclization behavior in any way.

5.4 Reference electrodes

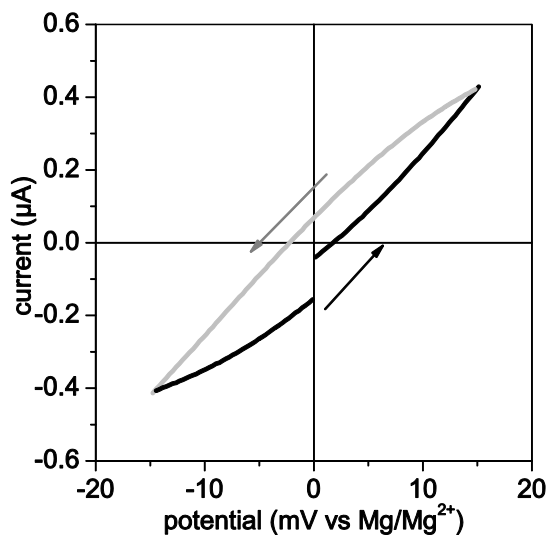


Fig. 45 Polarization sweep of the Mg reference electrode in 0.25 M APC solution at 1.0 mV s⁻¹ sweep rate.

To examine the utility of the Mg foil quasi-reference electrode a micro polarization test against the counter electrode in 0.25 M APC electrolyte was carried out. The scan started anodically from 0.0 V, swept to 15 mV and then cycled to -15 mV and back again, with a scan rate of 1.0 mV s⁻¹.

The current showed a hysteresis loop with the potential. This loop is an indication for a polarizable electrode that should not be used as reference electrode [73]. This hysteresis has an impact of a few mV on the exact determination of potential values. Therefore, further measurements need to be done with non-polarizable reference

electrodes. Hence, we suggest to use an Ag/Ag⁺ couple as reference electrode of the first kind. The setup could be as follows: a Ag wire is dipped into a 0.01 M AgBF₄/0.1 M TBAHFP in THF solution and frit connects it to a 0.1 M TBAHFP solution in THF. The last part of the electrode arrangement is a Haber-Luggin capillary filled with the THF electrolyte.

For a precise determination of peak potentials for the magnesium deposition/dissolution process, measurements with internal potential standards like ferrocene or cobaltocene are useful. Since the standard potential of ferrocene in THF ($E^\circ(\text{FcCp}_2^+/\text{FcCp}_2) = 0.45 \text{ V vs. SCE}$ [74]) is quite positive (3.09 V vs. Mg/Mg^{2+}) its redox peaks are superimposed on the electrolyte decomposition. Therefore the better internal potential standard for the investigated electrolytes is $\text{CoCp}_2^+/\text{CoCp}_2$ ($E^\circ = -0.90 \text{ V vs. SCE}$ in THF [74]). Since the electrochemical reaction of the magnesium deposition/dissolution occurs at very negative potentials, the redox couple $\text{CoCp}_2/\text{CoCp}_2^-$ could be observed as well ($E^\circ = -2.04 \text{ V vs. SCE}$ in THF [74]).

6 Summary and conclusion

This master thesis deals with the search of electrolytes for the rechargeable Mg-ion battery with anodic stabilities >3 V (vs. Mg/Mg²⁺) and coulombic efficiencies >90 %. The preparation of the boron based electrolyte involved the synthesis of commercially non available triarylboranes. Furthermore, the cyclization behavior of anode materials in a suitable electrolyte has been tested.

Three THF based electrolytes, namely all phenyl complex (APC), tris(pentafluorophenyl)borane-phenylmagnesiumchloride (BCF-PhMgCl) and magnesium aluminium chloride complex (MACC) have been prepared for the investigation by cyclic voltammetry, chronoamperometry and multinuclear NMR. Since APC and BCF-PhMgCl both include the Grignard reagent PhMgCl, it was also characterized by the mentioned electrochemical methods.

The preparation of boron electrolytes required the synthesis of triarylboranes. The synthesis described by Brown *et al.* [61] did not bring about the desired yield and purity of the product. Replacing the in situ generated Grignard reagent by commercially available PhMgCl and using trimethylborate instead of boron trifluoride lead to better yield but the purity was still insufficient. Since all aryl boranes are water and air sensitive most likely traces of water are responsible for the insufficient yield.

The results of the electrochemical investigation of the electrolytes and the Grignard reagent are summarized in Table 12:

Table 12: Electrochemical properties of the investigated electrolytes on Pt-electrode.

Electrolyte	1 M PhMgCl	0.25M APC 1:2	0.2 M BCF- PhMgCl 1:2	0.2 M BCF- PhMgCl 1:3	0.04 M ² MACC 1:2
anodic stability (vs. Mg/Mg ²⁺)	≥ 2.1 V	≥ 2.9 V	≥ 2.05 V	≥ 2.40 V	≥ 3.0 V
highest current efficiency	≤ 99 %	≤ 99 %	≤ 62 %	≤ 86 %	≤ 57 %

All electrolytes showed reversible electrodeposition of magnesium except the 0.2 M BCF-PhMgCl 1:1 solution (hence, it is not listed). The best results concerning the electrolyte potential limit in combination with the reversibility were achieved with the 0.25 M APC electrolyte. The 0.2 M BCF-PhMgCl 1:3 showed promising results but the anodic limit predicted in the literature [32] could not be reproduced. Most likely this was due to the existing impurities of the starting material B(C₆F₅)₃ needed for the electrolyte preparation.

² estimated value based on [34]

The MACC solution revealed the highest anodic stability but the current efficiency is the lowest. In addition, this electrolyte showed a high overpotential for magnesium deposition (≤ 900 mV). This overpotential together with the low current efficiency suggests the formation of a blocking layer on the electrode surface. NMR studies of MACC identified AlCl_4^- to be the only anionic species being responsible for the high stability. This anion is also part of the equilibrium in 0.25 M APC electrolyte [63] which showed about the same stability.

An interesting effect was encountered when the Grignard containing electrolytes were tested on glassy carbon and platinum electrodes. Better performance on the glassy carbon electrode was expected because there are several intermetallic phases of Pt and Mg known. But it seems platinum does not form surface alloys with electrodeposited magnesium. In contrast glassy carbon seems to react with electrochemically generated decomposition products of the Grignard reagent in the electrolyte. The radicals in the solution might electrograft on the surface and change its electrochemical properties.

The different anode materials – Mg 99.9 %, MgGd (1.5 % Gd) , MgGdZn (0.5 % Gd, 1.5 % Zn) – exhibited good cycling capability, but for each alloy an overvoltage in the first cycle was observed. This effect might be due to surface passivation, even though the materials were ground and handled in the glovebox. The alloying elements Gd or Zn do not seem to have an impact on the cyclization behavior.

In conclusion, the following should be considered with regard to the synthesis: The resulting boron species depends on the used solvent. While diethylether favors the formation of triaryl boranes, whereas in THF tetracoordinated anions are more likely formed. In addition there is a difference in the solubility of the occurring salts $\text{FMgBr}/\text{FMgCl}$ and CH_3OMgCl . While $\text{FMgBr}/\text{FMgCl}$ precipitates, CH_3OMgCl nearly does not. This fact is crucial for the purification of triarylboranes and since arylborane compounds are water-sensitive, the exclusion of water and air is most important.

Concerning further electrochemical experiments a reliable reference electrode has to be used to ensure a more precise determination of potentials. For the MACC electrolyte the cyclic voltammetry experiment should be repeated on a Mg anode, which might help to improve the reversibility of the magnesium deposition/dissolution reaction. Moreover, an electrochemical study on the impact of oxygen should be considered by using unalloyed Mg as anode material with known concentrations of oxygen. For these studies, however, it is also necessary to improve the grinding and polishing procedure for Mg. Since the electrochemical experiments are carried out in the glovebox, a chemical etching step with a non-aqueous etching solution could be performed as the last step in the glovebox before the electrochemical measurements to remove the possibly formed passive layer on the Mg surface.

The results obtained herein, show that a secondary battery based on magnesium is possible since the APC solution shows a nearly completely reversible deposition/

dissolution of Mg and a high potential window vs. the Mg anode. But still a lot of research will be needed to gain more information on the diffusion process of the Mg ion in solution and to better understand the deposition/dissolution process of the active Mg ion species to find the optimal electrolyte for battery applications.

REFERENCES

- [1] Dhameja, S. (2002). *Electric vehicle battery systems*. Boston: Newens.
- [2] Sterner, M., & Stadler, I. (2014). *Energiespeicher - Bedarf, Technologien, Integration*. Berlin Heidelberg: Springer-Verlag.
- [3] Dell, R., Moseley, P., & Rand, D. (2014). *Towards sustainable road transport*. Oxford: Academic Press.
- [4] Crompton, T. (2000). *Battery reference book* (3rd ed.). Oxford: Newens.
- [5] Aurbach, D., Gofer, Y., Lu, Z., Schechter, A., Chusid, O., Gizbar, H., et al. (2001). A short review on the comparison between Li battery systems and rechargeable magnesium battery technology. *Journal of Power Sources*, 97-98 (0), 28-32.
- [6] Glied, M. (1995-2006). *Uniterra-Berlin*. Retrieved November 18, 2014, from <http://www.uniterra.de/rutherford/>
- [7] Aurbach, D., Lu, Z., Schechter, A., Gofer, Y., Gizbar, H., Turgeman, R., et al. (2000). Prototype systems for rechargeable magnesium batteries. *Nature*, 407 (6805), 724-727.
- [8] Liang, Y., Feng, R., Yang, S., Ma, H., Liang, J., & Chen, J. (2011). Rechargeable Mg batteries with graphene-like MoS₂ cathode and ultrasmall Mg nanoparticle anode. *Advanced Materials*, 23 (5), 640-643.
- [9] Chusid, O., Gofer, Y., Gizbar, H., Vestfrid, Y., Levi, E., Aurbach, D., et al. (2003). Solid-state rechargeable magnesium batteries. *Advanced Materials*, 15 (7-8), 627-630.
- [10] Arthur, T. S., Singh, N., & Matsui, M. (2012). Electrodeposited Bi, Sb and Bi_{1-x}Sb_x alloys as anodes for Mg-ion batteries. *Electrochemistry Communications*, 16 (1), 103-106.
- [11] Singh, N., Arthur, T. S., Ling, C., Matsui, M., & Mizuno, F. (2013). A high energy-density tin anode for rechargeable magnesium-ion batteries. *Chemical Communications*, 49 (2), 149-151.
- [12] Levi, E., Gofer, Y., & Aurbach, D. (2009). On the way to rechargeable Mg batteries: The challenge of new cathode materials. *Chemistry of Materials*, 22 (3), 860-868.
- [13] Gregory, T. D., Hoffman, R. J., & Winterton, R. C. (1990). Nonaqueous electrochemistry of magnesium. Applications to energy storage. *Journal of the Electrochemical Society*, 137 (3), 775-80.
- [14] Novak, P., & Desilvestro, J. (1993). Electrochemical insertion of magnesium in metal oxides and sulfides from aprotic electrolytes. *Journal of The Electrochemical Society*, 140 (1), 140-144.
- [15] Kamioka, N., Ichitsubo, T., Uda, T., Imashuku, S., Taninouchi, Y., & Matsubara, E. (2008). Synthesis of spinel-type magnesium cobalt oxide and its electrical conductivity. *Materials Transaction*, 49 (4), 824-828.
- [16] Ichitsubo, T., Adachi, T., Yagi, S., & Doi, T. (2011). Potential positive electrodes for high-voltage magnesium-ion batteries. *Journal of Materials Chemistry*, 21 (32), 11764-11772.
- [17] Makino, K., Katayama, Y., Miura, T., & Kishi, T. (2001). Electrochemical insertion of magnesium to Mg_{0.5}Ti₂(PO₄)₃. *Journal of Power Sources*, 99 (1-2), 66-69.
- [18] Saha, P., Datta, M. K., Velikokhatnyi, O. I., Manivannan, A., Alman, D., & Kumta, P. N. (2014). Rechargeable magnesium battery: Current status and key challenges for the future. *Progress in Materials Science* (66), 1-86.
- [19] Feng, Z., Yang, J., NuLi, Y., & Wang, J. (2008). Sol-gel synthesis of Mg_{1.03}Mn_{0.97}SiO₄ and its electrochemical intercalation behavior. *Journal of Power Sources*, 184 (2), 604-609.
- [20] Kim, H. S., Arthur, T. S., Allred, G. D., Zajicek, J., Newman, J. G., Rodnyansky, A. E., et al. (2011). Structure and compatibility of a magnesium electrolyte with a sulphur cathode. *Nature Communications*, 2, 427.
- [21] Levi, E., Gershinshy, G., Aurbach, D., Isnard, O., & Ceder, G. (2009). New insight of the unusually high ionic mobility in chevrel phases. *Chemistry of Materials*, 21, 1390-1399.

- [22] Levi, M., & Aurbach, D. (2005). A comparison between intercalation of Li and Mg ions into the model chevrel phase compound ($M_xMo_6S_8$): Impedance spectroscopic studies. *Journal of Power Sources*, 146 (1-2), 349-354.
- [23] Levi, M. D., Lancry, E., Gizbar, H., Lu, Z., Levi, E., Gofer, Y., et al. (2004). Kinetic and thermodynamic studies of Mg^{2+} and Li^+ ion insertion into the Mo_6S_8 chevrel phase. *Journal of The Electrochemical Society*, 151 (7), A1044-A1051.
- [24] Pereira-Ramos, J., Messina, R., & Perichon, J. (1987). Electrochemical formation of a magnesium vanadium bronze $Mg_xV_2O_5$ in sulfone-based electrolytes at $150^\circ C$. *Journal of Electroanalytical Chemistry and Interfacial Electrochemistry*, 218 (1-2), 241-249.
- [25] Shklover, V., Haibach, T., Ried, F., Nesper, R., & Novak, P. (1996). Crystal structure of the product of Mg^{2+} insertion into V_2O_5 single crystals. *Journal of Solid State Chemistry*, 123 (2), 317-323.
- [26] Makino, K., Katayama, Y., Miura, T., & Kishi, T. (2002). Preparation and electrochemical magnesium insertion behaviors of $Mg_{0.5+y}(MeyTiy)_2(PO_4)_3$ (Me = Cr, Fe). *Journal of Power Sources*, 112 (1), 85-89.
- [27] Lu, Z., Schechter, A., Moshkovich, M., & Aurbach, D. (1999). On the electrochemical behavior of magnesium electrodes in polar aprotic electrolyte solutions. *Journal of Electroanalytical Chemistry*, 466 (2), 203-217.
- [28] Lossius, L. P., & Emmenegger, F. (1996). Plating of magnesium from organic solvents. *Electrochimica Acta*, 41 (3), 445-447.
- [29] Guo, Y., Yang, J., NuLi, Y., & Wang, J. (2010). Study of electronic effect of Grignard reagents on their electrochemical behavior. *Electrochemistry Communications*, 12 (12), 1671-1673.
- [30] Yoo, H. D., Shterenberg, I., Gofer, Y., Gershinshy, G., Pour, N., & Aurbach, D. (2013). Mg rechargeable batteries: an on-going challenge. *Energy Environmetal Science*, 6, 2265-2279.
- [31] Mizrahi, O., Amir, N., Pollak, E., Chusid, O., Marks, V., Gottlieb, H., et al. (2008). Electrolyte solutions with a wide electrochemical window for rechargeable magnesium batteries. *Journal of the Electrochemical Society*, 155 (2), A103-A109.
- [32] Muldoon, J., Bucur, C. B., Oliver, A. G., Sugimoto, T., Matsui, M., Kim, H. S., et al. (2012). Electrolyte roadblocks to a magnesium rechargeable battery. *Energy and Environmental Science*, 5 (3), 5941-5950.
- [33] Guo, Y., Zhang, F., Yang, J., & Wang, F. (2012). Electrochemical performance of novel electrolyte solutions based on organoboron magnesium salts. *Electrochemistry Communications*, 18 (0), 24-27.
- [34] Liu, T., Shao, Y., Li, G., Gu, M., Hu, J., Xu, S., et al. (2014). A facile approach using $MgCl_2$ to formulate high performance Mg^{2+} electrolytes for rechargeable Mg batteries. *Journal of Materials Chemistry A: Materials for Energy and Sustainability*, 2 (10), 3430-3438.
- [35] Doe, R. E., Han, R., Hwang, J., Gmitter, A. J., Shterenberg, I., Yoo, H. D., et al. (2014). Novel, electrolyte solutions comprising fully inorganic salts with high anodic stability for rechargeable magnesium batteries. *Chemical Communications*, 50 (2), S. 243-245.
- [36] Wang, F., Guo, Y., Yang, J., Nuli, Y., & Hirano, S. (2012). A novel electrolyte system without a Grignard reagent for rechargeable magnesium batteries. *Chemical Communications*, 48 (87), 10763-10765.
- [37] NuLi, Y., Yang, J., & Wang, P. (2006). Electrodeposition of magnesium film from BMIMBF₄ ionic liquid. *Applied Surface Science*, 252 (23), 8086-8090.
- [38] Zhao, Q. S., NuLi, Y., Nasiman, T., Yang, J., & Wang, J. (2012). Reversible deposition and dissolution of magnesium from imidazolium-based ionic liquids. *International Journal of Electrochemistry*, 2012, 8.
- [39] Endres, F., Abbott, A., & MacFarlane, D. (Eds.). (2008). *Electrodeposition from ionic liquids*. Weinheim: WILEY-VCH Verlag.

- [40] Kakibe, T., ya Hishii, J., Yoshimoto, N., Egashira, M., & Morita, M. (2012). Binary ionic liquid electrolytes containing organo-magnesium complex for rechargeable magnesium batteries. *Journal of Power Sources*, 203 (0), 195-200.
- [41] Patrick, A., Glasse, M., Latham, R., & Linford, R. (1986). Novel solid state polymeric batteries. *Solid State Ionics*, 18-19, Part 2 (0), 1063-1067.
- [42] Yang, L. L., McGhie, A. R., & Farrington, G. C. (1986). Ionic conductivity in complexes of poly(ethylene oxide) and MgCl₂. *Journal of The Electrochemical Society*, 133 (7), 1380-1385.
- [43] Liebenow, C. (1998). A novel type of magnesium ion conducting polymer electrolyte. *Electrochimica Acta*, 43 (10-11), 1253-1256.
- [44] Liebenow, C., & Mantey, S. (2003). Preparation of solutions of amidomagnesium chlorides in poly(ethylene oxide) and their characterization by conductivity measurements. 7 (5), 313-316.
- [45] Kumar, Y., Hashmi, S., & Pandey, G. (2011). Ionic liquid mediated magnesium ion conduction in poly(ethylene oxide) based polymer electrolyte. *Electrochimica Acta*, 56 (11), 3864-3873.
- [46] Girish Kumar, G., & Munichandraiah, N. (2002). Poly(methylmethacrylate)-magnesium triflate gel polymer electrolyte for solid state magnesium battery application. *Electrochimica Acta*, 47 (7), 1013-1022.
- [47] Girish Kumar, G., & Munichandraiah, N. (2000). A gel polymer electrolyte of magnesium triflate. *Solid State Ionics*, 128 (1-4), 203-210.
- [48] Girish Kumar, G., & Munichandraiah, N. (2001). Solid-state rechargeable magnesium cell with poly(vinylidene fluoride)-magnesium triflate gel polymer electrolyte. *Journal of Power Sources*, 102 (1-2), 46-54.
- [49] Aravindan, V., Karthikaselvi, G., & Vickraman, P. N. (2009). Polyvinylidene fluoride-based novel polymer electrolytes for magnesium-rechargeable batteries with Mg(CF₃SO₃)₂. *Journal of Applied Polymere Science*, 112 (5), 3024-3029.
- [50] Yoshimoto, N., Shirari, T., & Morita, M. (2005). A novel polymeric gel electrolyte system containing magnesium salt with ionic liquid. *Electrochimical Acta*, 50, 3866-3871.
- [51] Oh, J. S., Ko, J. M., & Kim, D. W. (2004). Preparation and characterization of gel polymer electrolytes for solid state magnesium batteries. *Electrochimica Acta*, 50 (2-3), 903-906.
- [52] Narayanan, N. S., Ashok, R. B., & Sampath, S. (2009). Magnesium ion conducting, room temperature molten electrolytes. *Electrochemical Communications*, 11 (13), 2027-2031.
- [53] Benn, R., & Rufinska, A. (1986). Hochauflösende Metallkern-NMR-Spektroskopie von Organometallverbindungen. *Angewandte Chemie*, 98 (10), 851-871.
- [54] Eaton, G. R. (1969). NMR of boron compounds. *Journal of Chemical Education*, 46 (9), 547-556.
- [55] Popov A.I., H. K. (1991). *Modern NMR techniques and their application in chemistry*. New York: Marcel Dekker Inc.
- [56] Cole Research Group. (2014). *SDSU Department of Chemistry and Biochemistry*. Abgerufen am 30. November 2014 von <http://www.chemistry.sdsu.edu/research/BNMR/>
- [57] Mason, J. (1987). *Multinuclear NMR* (1st ed.). New York: Plenum Press.
- [58] Espinet, P., Albeniz, A. C., Casares, J. A., & M. I., J. M. (2008). ¹⁹F NMR in organometallic chemistry: Applications of fluorinated aryls. *Coordination Chemistry Reviews*, 252 (21-22), 2180-2208.
- [59] Dolbier, W. R. (2009). *Guide to fluorine NMR for organic chemists*. New Jersey: John Wiley & Sons Inc.
- [60] Bard, A., & Faulkner, L. (2001). *Electrochemical methods: Fundamentals and applications*. New York: John Wiley & Sons Inc.
- [61] Brown, H., & Racherla, U. (1986). Organoboranes. A convenient, highly efficient synthesis of triarylboranes via a modified organometallic route. *Journal of Organic Chemistry*, 51 (4), 427-432.

- [62] Magerlein, B., & Schneider, W. (1969). 4-Phenylazodiphenylamine, a novel reagent for the determination Grignard reagent and its use in the preparation of 6 α -¹⁴C-methylhydrocortisone. *The Journal of Organic Chemistry*, 34 (4), 1179-1180.
- [63] Pour, N., Gofer, Y., Major, D. T., & Aurbach, D. (2011). Structural analysis of electrolyte solutions for rechargeable Mg batteries by stereoscopic means and DFT calculations. *Journal of the American Chemical Society*, 133 (16), 6270-6278.
- [64] Hermanek, S. (1992). Boron-11 NMR spectra of boranes, main-group heteroboranes, and substituted derivatives. Factors influencing chemical shifts of skeletal atoms. *Chemical Reviews*, 92 (2), 325-362.
- [65] Lucht, B., Henderson, W. A., Jow, T. R., & Ue, M. (Eds.). (2011). *Non-aqueous electrolytes for lithium batteries*. New Jersey: The Electrochemical Society.
- [66] McCreery, R. L. (2008). Advanced carbon electrode materials for molecular electrochemistry. *Chemical Reviews*, 108 (7), 2646-2687.
- [67] Belanger, D., & Pinson, J. (2011). Electrografting: a powerful method for surface modification. *Chemical Society Reviews*, 40 (7), 3995-4048.
- [68] Barile, C. J., Spatney, R., Zavadil, K. R., & Gewirth, A. A. (2014). Investigating the Reversibility of in Situ Generated Magnesium Organohaloaluminates for Magnesium Deposition and Dissolution. *The Journal of Physical Chemistry C*, 118 (20), 10694-10699.
- [69] Benmayza, A., Ramanathan, M., Arthur, T. S., Matsui, M., Mizuno, F., Guo, J., et al. (2013). Effect of electrolytic properties of a magnesium organohaloaluminate electrolyte on magnesium deposition. *Journal of Physical Chemistry C*, 117 (51), 26881-26888.
- [70] Lehmann, M., Schulz, A., & Villinger, A. (2009). Bissilylated halonium ions: [Me₃Si-X-SiMe₃][B(C₆F₅)₄] (X = F, Cl, Br, I). *Angewandte Chemie, International Edition*, 48 (40), 7444-7447.
- [71] Tian, J., Wang, S., Feng, Y., Li, J., & Collins, S. (1999). Borane-functionalized oxide supports: Development of active supported metallocene catalysts at low aluminoxane loading. *Journal of Molecular Catalysis A: Chemical*, 144 (1), 137-150.
- [72] Barile, C. J., Barile, E. J., Zavadil, K. R., & Nuzzo, R. G. (2014). Electrolytic conditioning of a magnesium aluminum chloride complex for reversible magnesium deposition. *The Journal of Physical Chemistry C*, 118, 27623-27630.
- [73] Southampton Electrochemistry Group. (1985). *Instrumental Methods in Electrochemistry*. Chichester: Ellis Horwood Ltd.
- [74] Bard, A. L., Gracia, E., Kukharenko, S., & Strelets, V. V. (1993). Electrochemistry of metallocenes at very negative and very positive potentials. Electrogeneration of Cp₂Co²⁺, Cp₂Co²⁻ and Cp₂Ni²⁻ species. *Inorganic Chemistry*, 32 (16), 3528-3531.
- [75] Miller, S. (2012). www.chemistryviews.org. Retrieved November 24, 2014, from http://www.chemistryviews.org/details/education/2538941/Tips_and_Tricks_for_the_Lab_Growing_Crystals_Part_3.html

LIST OF FIGURES

Fig.1.	Performance of different batteries in terms of specific energy and energy density [3].	2
Fig.2.	ORTEP plot of $[\text{Mg}_2(\mu - \text{Cl})_3 \cdot 6\text{THF}] + [32]$.	6
Fig.3.	Boron complex with different aryl groups.	7
Fig.4.	Shifts of ^{11}B molecules relative to $\text{BF}_3 \cdot \text{OEt}_2$ [56].	11
Fig.5.	Shifts of different coordinated aluminum compounds (ref. $\text{Al}(\text{H}_2\text{O})_6^{3+}$) [57].	12
Fig.6.	Triangular potential wave function (a), cyclic voltammogram (b) [60].	13
Fig.7.	Potential step (a), concentration gradient over time (b) [60].	13
Fig.8.	Vacuum sublimation apparatus [73].	20
Fig.9.	Measurement cell for electrolyte characterization.	21
Fig.10.	Mg-alloy electrode disk diameter $d = 10$ mm.	22
Fig.11.	^{11}B NMR spectrum of the halide approach at 96.3 MHz, 25°C, external lock signal: D_2O .	23
Fig.12.	^{11}B NMR spectrum of the Grignard approach with trimethylborate adduct at 96.3 MHz, 25°C, external lock signal: D_2O .	24
Fig.13.	HPLC analysis of the standard solution (a) and the electrolyte solution (b), prepared according to procedure 4.2.2 with trimethylborate.	24
Fig.14.	^{11}B NMR spectrum of the Grignard approach with $\text{BF}_3 \cdot \text{OEt}_2$ adduct at 96.3 MHz, 25°C, external lock signal: D_2O .	25
Fig.15.	Functional groups on a graphite surface [66].	27
Fig.16.	Cyclic voltammograms of continuously repeated 6 cycles of 1 M PhMgCl in THF on Pt electrode, $\nu = 50$ mV/s at 30°C; start from the OCP = 1.1 V in positive direction.	28
Fig.17.	Cyclic voltammograms of 1 M PhMgCl at Pt disk electrode with scan rates between 10-100 mV/s (top) and RDE voltammograms with scan rates between 5-50 mV/s (bottom); start from the OCP in positive direction	29
Fig.18.	CV for Mg deposition/dissolution from 1 M PhMgCl electrolyte on Pt electrodes at $\nu = 50$ mV/s and 30°C. The cathodic limit varies from -0.5 V to -0.8 V; start from the OCP = 1.1 V in positive direction.	30
Fig.19.	Rotation disk voltammograms at $\nu = 50$ mVs $^{-1}$ of 1 M PhMgCl on Pt at 30°C. The rotation rates vary from 0-1500 rpm: start from the OCP in positive direction.	31
Fig.20.	Chronoamperogram (a) and chronocoulogram (b) of 1 M PhMgCl at different potentials.	32
Fig.21.	CV of continuously repeated 10 cycles of 0.25 M APC in THF on Pt electrode, $\nu = 50$ mV/s at 30°C (OCP = 2.05 V)	33
Fig.22.	Cyclic voltammograms of 0.25 M APC on Pt at 30°C. The scan rates vary from 10-100 mV s $^{-1}$.	34
Fig.23.	CV for Mg deposition/dissolution of 0.25 M APC on Pt electrodes at $\nu = 50$ mV/s and 30°C. The cathodic limit varies from -0.5 V to -1.0 V.	34
Fig.24.	Chronoamperogram (a) and chronocoulogram (b) of 0.25 M APC at different potentials.	35
Fig.25.	Anson plot for different Mg deposition potentials (left). Diffusion coefficient dependency on the applied potential (right).	36
Fig.26.	Cottrell plot for different Mg deposition potentials (left). Diffusion coefficient dependency on the applied potential (right).	36
Fig.27.	Cyclic voltammograms of three different BCF-PhMgCl ratios on Pt at $\nu = 50$ mV s $^{-1}$ at $T = 30^\circ\text{C}$. Inset shows the enlargement of the oxidation region to highlight the anodic stability of different ratios of the boron based electrolyte.	37
Fig.28.	BCF-PhMgCl electrolyte: different ratios of tris(pentafluorophenyl) borane and Grignard compound.	37

- Fig.29. Cyclic voltammograms of 0.2 M BCF-PhMgCl 1:3 (top) and 1:2 (bottom) electrolyte on Pt at 30°C. The scan rates vary from 5-100 mV s⁻¹ for the 1:3 ratio and from 25-100 mV s⁻¹ for the 1:2 ratio. 38
- Fig.30. CV for Mg deposition/dissolution from 0.2 M BCF:PhMgCl 1:3 (top) and 1:2 (bottom) on Pt electrodes at $\nu = 10$ mV/s and 30°C. The cathodic limit varies from -0.4 V to -1.0 V. The figures on the right display the corresponding CE of each measurement. 39
- Fig.31. The spectra on the left display the ¹⁹F NMR of different ratios of BCF-PhMgCl, the spectra on the right show the ¹¹B NMR results. 39
- Fig.32. ¹⁹F NMR spectrum of tris(pentafluorophenyl)borane in CD₂Cl₂. 41
- Fig.33. Cyclic voltammogram of continuously repeated 10 scans of 1:2 MACC in THF on Pt electrode, $\nu = 50$ mV/s at 30°C (OCP = 1.7 V). The inset on top shows the current efficiency of each cycle while the one on the bottom displays current of the side reaction. 42
- Fig.34. Enlargement of the oxidation region to highlight the anodic stability of MACC, $\nu = 50$ mV s⁻¹, Pt, 30°C (a) and enlargement of the cathodic limit to display the onset potential for the deposition of magnesium, $\nu = 50$ mV s⁻¹, Pt, 30°C (b). 42
- Fig.35. Cyclic voltammograms of sat. MACC on Pt working electrode with scan rates between 1-100 mV/s. 43
- Fig.36. Cyclic voltammograms for Mg deposition/dissolution of sat. MACC electrolyte on Pt electrodes at $\nu = 50$ mV/s and 30°C. The cathodic limit varies from -0.9 V to -1.2 V. 43
- Fig.37. ²⁷Al NMR spectrum of MACC at 78.2 MHz, 25°C, external lock signal D₂O. 44
- Fig.38. Three voltammetric cycles of Mg 99.9 % starting in negative direction (a) and three voltammetric cycles starting in positive direction (b) in 0.25 M APC solution, $\nu = 10$ mVs⁻¹ at 30°C. 45
- Fig.39. Cyclization experiments of Mg 99.9 % in 0.25 M APC at 100, 50 and 10 mVs⁻¹. For a better visualization of each cycle, cycle 2 and 3 have been shifted upward by a constant current density of 5 mA/cm². 46
- Fig.40. Current efficiency of Mg 99.9 % for the last two cycles at different scan rates. 47
- Fig.41. Cyclization experiments of MgGd in 0.25 M APC at 100, 50 and 10 mVs⁻¹. For a better visualization of each cycle, cycle 2 and 3 have been shifted upward by a constant current density of 5 mA/cm². 48
- Fig.42. Current efficiency of MgGd for the last 2 cycles at different scan rates. 48
- Fig.43. Cyclization experiments of MgGdZn in 0.25 M APC at 100, 50 and 10 mVs⁻¹. For a better visualization of each cycle, cycle 2 and 3 have been shifted upward by a constant current density of 5 mA/cm². 49
- Fig.44. Current yield of MgGdZn for the last 2 cycles at different scan rates. 50
- Fig.45. Polarization sweep of the Mg reference electrode in 0.25 M APC solution at 1.0 mV s⁻¹ sweep rate. 50

CURRICULUM VITAE

Alexandra Ploner

Date of Birth: 10th of July 1989, Zams

Austria

Education

- 10/2012-01/2015 **Technical University of Graz**
Master of Science in Advanced Materials Science
- 10/2008-8/2012 **Leopold-Franzens University of Innsbruck**
Bachelor of Science in Chemistry
- 1999 - 2007
Wirtschaftskundliches Realgymnasium der Ursulinen
Innsbruck (grammar school)
- 1995 – 1999
Volksschule Dreieiligen/ Volksschule Angergasse
(elementary school)

Work experience

- 12/2012-2/2014 **Lab technician, A.Heuberger Eloxal GmbH, Graz Austria**
chemical analysis of aluminum anodizing baths

Skills

- Languages **German (native), Englisch (fluent)** (First Certificate)
- Computer MS Word, MS Excel, MS Power Point, Origin
- Hobbies **Ninepin bowling** (Sportkegeln)
former member of Austria's national squad